UiT THE ARCTIC UNIVERSITY OF NORWAY

Department of Physics and Technology

"Speckle filtering of Polarimetric SAR data"

—

Stefano Anzilotti

FYS-3941 Master's thesis in applied physics and mathematics - June 2017

Abstract

In the field of *Remote Sensing* the main device, used to obtain the surface images, are the so-called *Synthetic Aperture Radar*. This systems are devices able to catch high-resolution images, which keep peculiar informations about the observed surface. Through the use of a *Radar*, mounted on board of a spaceborne or airborne vehicle, large overflow areas are electromagnetically radiating. The electromagnetic answer of the illuminated surface under discussion, is then analyzed in such a way to extract the wished informations. This kind of image acquisition presents an intrinsic trouble generated by the set of electromagnetic waves, which are interacting each other, on the path from the target to the receiver system. The trouble is well-known as *Speckle* and it will be the main topic of this thesis project.Over the last 30 years, several algorithms able to significantly reduce the trouble effect have been implemented. However, trouble reduction, is done to the detriment of the preserved information. On this basis, an equal important research is to *evaluate* in detail, as more as possible, the speckle filtering performance and moreover which informations are preserved and which are degraded. For this reason, a comparison between the *filtered images* and the *untroubled images* may be useful, but as it has been said above, signal and trouble are inseparable, therefore an untroubled version of the acquired image is not achievable.To work around the problem, has been generated a synthetic image where the speckle contribute is absent, using some representative sample extracted from a real SAR image, that in this case is the well-known SAR image over the San Francisco Bay (CA). Thus, based on it, speckle contribute has been added on the image. Furthermore, to make the simulation more realistic, it has been added *texture*, which may represent high density forest or urban area, as well as *target point*, which may represent naval ships at open sea, or more generally, small dimension object anywhere.Subsequently, two types of parameters have been implemented for the evaluation of the information preserved. First, *polarimetric preservation parameters*, which express a measurement about *intensity* of *speckle contribute* for each channel, *entropy*, *anisotropy*, *mean angle alpha* and the *polarimetric signature*. Second, *spatial preservation parameters*, which measure *edge preservation*, *target point preservation* and the *Equivalent Number of Look* of the filtered image. Next, a collection of test images has been stored with *Monte Carlo Method* and several filters through the platform *PolSARpro* have been applied. Each sample image has been evaluate in term of the parameters above presented. Finally, each filter has been applied to the real image in such a way to have the opportunity to highlight and to compares the conclusion obtained about the parameters and their respective filtered image.

Contents

List of Figures

List of Tables

List of Acronyms

Introduction 1

Since the humanity has the possibility to send technological equipment in the space or in the sky, a new perspective to observe and monitoring Earth's surface or atmosphere and the planetary system, is in continuous increase [1]. More specifically about Earth observation, the sensor catches information regarding global patterns, seasonal variations about surface of vegetation and ocean with the respective morphologic structure. Other informations acquirable are dynamics of clouds and near-surface wind. The field that studies this phenomena is called *remote sensing* and is defined as the acquisition of information about an object without being in physical contact with it. In the last forty years, this field, has been invaded about developments of electromagnetic technology, which are able to detect and measure details of the transmitted and reflected waves that contains the main information about the interaction of the medium. The technology on which remote sensing has based its roots is the *radar system* concept. Radar history borns in military contest where the presence of impressive economic resources is well-known. Precisely for this reason its scientific development has been majestic and quickly. Over the years, the *polarimetry* is became an important topic about radar acquisition. It uses the polarization of the electromagnetic waves as supplementary parameter in such a way to get more information about the target. Today, *Synthetic Aperture Radar* (SAR) represent the last generation of radars. Images are acquired by SARs, which are basically radar mounted on airborne or spaceborne vehicles. That radars emit pulses and use space variation of the platform, where they are allocated, to have a spatial sampling illumination of the target. The illumination time is normally a long interval, thus the system receives a large number of echoes from the target [2]. SARs are developed to acquire high quality spectra about observed surface or atmospheric. It means a direct identification of the surface or atmospheric composition. Multichannel imaging radars acquisition takes advantage of the concepts of *polarimetry* and *interferometry* for providing detailed maps of the surface morphology, the structure about the surface level as well as its motion [3]. In addition there are other advantages about the method wherewith the signal is obtained, that is the quickly coverage capability, of wide areas, that satellite or airplane are able to monitoring. This rapidity on large scale can follow the equally rapidity of phenomena that are changing, particularly in the atmosphere. Moreover, the acquisition for a longer period and the possibility to repeat the observation become essential in case as the observation of seasonal, annual, and longer-term changes such as polar ice cover, desert expansion, and tropical deforestation. The wide-scale synoptic coverage allows the observation and study of regional and continental-scale features such as plate boundaries and mountain chains.

1.1 Goals

As well described later in Chapter 3, the main problem that links all the images acquired as electromagnetic answers of the surface, is a trouble called *speckle*. As a general rule, the main goal could be thought as the best method to remove this kind of trouble, but this huge concepts has been divided below in concrete steps. The signal received and speckle are inseparable each other. Assuming to remove the trouble by filtering, it is not possible to have a clear comparison of the processed image and the original image.

- *First goal*: generating a ideal image which is speckle free in order to have the possibility to compare the filter performance than an image noiseless.
- *Second goal*: it comes immediately from the first goal, is to add a signal which can replicate the statistical behaviour of the speckle.
- *Third goal*: for making a realistic image, a further signal has been added to simulate the structure of urban and vegetation areas. This signal is called *texture*.
- Fourth goal: realizing parameters to compare the images processed by several filters.
- Future goal: making a new speckle filter and evaluate it in the same way as for the other.

Due to the limited time spent in the University of Tromsø, the future goal will be taken into account in the last version of this master thesis, which will be handed over at the University of Florence.

1.2 State of the Art

The master thesis work finds its main roots in two reference:

- *Analysis, Evaluation, and Comparison of Polarimetric SAR Speckle Filtering Techniques*, written by Samuel Foucher and Carlos López-Martínez [4].
- *Polarimetric Radar Imaging from Basics to Applications*, written by Jong-Sen Lee and Eric Pottier [5].

The first one is the article from which has been taken the main tasks of this master thesis. It reports a way to implement an ideal image with polarimetric property and then an further analysis of it by using new parameters which has been built specifically for that reason.

The second one is the book where has been taken the majority theory concepts, which have been indispensable to deep understand and to realize what has been achieved in the article above mentioned.

1.3 Thesis's Structure

In order to give to the reader a general view of the thesis work, a brief review of each chapter has been reported:

- Chapter 2: *Image Acquisition*.

  This chapter is essentially made for recalling the main concepts which will be used in the whole work. The concept analyzed are: *electromagnetic theory*, *radar theory*, *synthetic aperture radar* and *polarimetric synthetic aperture radar*.

- Chapter 3: *Speckle*.

  An integer chapter has been dedicated to explain the *Speckle* phenomena. Thus, it has been analyzed which kind of problems this disturbance manifest, his origin, his basic statistic and the data statistic of single-channel and multi-look data for both case of single channel and multi channel.

- Chapter 4: *PolSAR Data Simulation*.

  This chapter explains step-by-step how has been created the final synthetic image. The storing of the representative samples form the real image for create the synthetic image without speckle. The realization of a second image where the speckle contribute is present. A third image where has been added *texture* to get a more realistic case. The finally image where has been added target point useful for tasting the parameters used to evaluate the speckle filters.

- Chapter 5: *PolSAR Data Filters Analysis*.

  Next, it has been implemented eight parameters able to evaluate the information's preservation of speckle filters. *Polarimetric evaluation*: radiometric parameters, complex correlation parameters, incoherent decomposition parameters and co/cross - polar polarization signature parameters. *Spatial evaluation*: gradient preservation, edge preservation, point target preservation and equivalent number of look.

- Chapter 6: *Result*.

  Finally, in Chapter 6, has been shown all the result of the filtering operation of the synthetic image made in Chapter 4. For each filter there is a table which hold the numeric values of the parameters made in Chapter 5 and a radar chart to view the filter behaviour in relation to the parameters. Moreover the filtered images are shown.

Image Acquisition 2

2.1 Electromagnetic Theory

Phenomena of classical electromagnetism may be represented by a special set of equations, which are called *Maxwell's Equations* [6]:

$$
\begin{array}{llll}
\text{I} & \nabla \times \mathbf{E}(\mathbf{r},t) = -\dfrac{\partial \mathbf{B}(\mathbf{r},t)}{\partial t} & \text{III} & \nabla \cdot \mathbf{D}(\mathbf{r},t) = \rho(\mathbf{r},t) \\
\text{II} & \nabla \times \mathbf{H}(\mathbf{r},t) = \dfrac{\partial \mathbf{D}(\mathbf{r},t)}{\partial t} + \mathbf{J}(\mathbf{r},t) & \text{IV} & \nabla \cdot \mathbf{B}(\mathbf{r},t) = 0
\end{array}
\tag{2.1}
$$

where:

- $\mathbf{E}(\mathbf{r}, t)$ represents the *electric field intensity* $[V/m]$.
- $\mathbf{H}(\mathbf{r}, t)$ represents the *magnetic field intensity* $[A/m]$.
- $\mathbf{B}(\mathbf{r}, t)$ represents the *magnetic induction* $[Wb/m^2]$.
- $\mathbf{D}(\mathbf{r}, t)$ represents the *electric induction* $[C/m^2]$.
- $\mathbf{J}(\mathbf{r}, t)$ represents the *electric current density* $[A/m^2]$.
- $\rho(\mathbf{r}, t)$ represents the *volume charge density* $[C/m^3]$.
- $\mathbf{r}$ represents the *displacement vector* $[m]$.
- t represents the *time* $[s]$.

The first is Faraday's law of induction. The second is Ampére's law as amended by Maxwell to include the displacement current $\partial \mathbf{D}(\mathbf{r}, t)/\partial t$, which is essential in predicting the existence of propagating electromagnetic waves. Then the third and fourth are Gauss's laws for the electric and magnetic fields [7].

They somehow depend on each other and through a simple algebraic manipulation it is possible to obtain the well-known *charge continuity equation*:

$$\nabla \cdot \mathbf{J}(\mathbf{r}, t) + \frac{\partial \rho(\mathbf{r}, t)}{\partial t} = 0 \tag{2.2}$$

In the wave propagation problems, ρ and $\mathbf{J}$ can be seen as the sources of the electromagnetic field. For wave propagation problems, these densities are localized in space; for example, the are restricted to flow on an antenna. The generated electric and magnetic fields are radiated away from the sources and propagate, to large distances, to the receiving antennas. Talking about *away from the sources* in other words means *source-free regions of space*, where Maxwell's equations take the simpler form:

$$\begin{array}{llll} \text{I} & \nabla \times \mathbf{E}(\mathbf{r},t) = -\dfrac{\partial \mathbf{B}(\mathbf{r},t)}{\partial t} & \text{III} & \nabla \cdot \mathbf{D}(\mathbf{r},t) = 0 \\ \text{II} & \nabla \times \mathbf{H}(\mathbf{r},t) = \dfrac{\partial \mathbf{D}(\mathbf{r},t)}{\partial t} + \mathbf{J}(\mathbf{r},t) & \text{IV} & \nabla \cdot \mathbf{B}(\mathbf{r},t) = 0 \end{array} \tag{2.3}$$

Coming back to the example above, a time-varying current $\mathbf{J}(\mathbf{r},t)$ on an antenna generates a circulating and time-varying magnetic field $\mathbf{H}(\mathbf{r},t)$, which according to Faraday's law generates a circulating electric field $\mathbf{E}(\mathbf{r},t)$, which according to Ampére's law generates a magnetic field, and so on.

For an easier notation, the dependences about the *displacement vector* and *time* will be omitted from now on.

2.1.1 Lorentz Force

In case of an environment which manifests electric and magnetic field **E** and **B**, a charge q, moving with velocity v, is subjected to a Lorentz's force given by:

$$\mathbf{F} = q(\mathbf{E} + v \times \mathbf{B}) \tag{2.4}$$

Moreover, the *Lorentz force equation*, links all the electromagnetic and mechanic phenomena in the free space. Current distributions **J** and volume charge ρ are subject to forces in the presence of electromagnetic fields. The force per unit volume on **J** and ρ is given by:

$$\mathbf{f} = \rho \cdot \mathbf{E} + \mathbf{J} \times \mathbf{B} \tag{2.5}$$

where **f** represents the *density force*, measured in $[N/m^3]$.

2.1.2 Constitutive Relations

Induction densities and field intensities are related by so-called *constitutive relations* [8]:

$$\begin{aligned} \mathbf{D} &= \epsilon_0 \mathbf{E} \\ \mathbf{B} &= \mu_0 \mathbf{H} \end{aligned} \tag{2.6}$$

where ϵ_0 is the *permittivity* and μ_0 the *permeability* of vacuum. Their values are:

$$\begin{aligned} \epsilon_0 &= 8.854 \times 10^{-12} \quad [farad/m] \\ \mu_0 &= 4\pi \times 10^{-7} \quad [henry/m] \end{aligned} \tag{2.7}$$

Taking into account a simple *homogeneous* [1] *isotropic* [2] *dielectric or magnetic* materials and assuming *low frequency* [3] case, the constitutive relations are:

$$\begin{aligned} \mathbf{D} &= \epsilon \mathbf{E} \\ \mathbf{B} &= \mu \mathbf{H} \end{aligned} \tag{2.8}$$

[1] An homogeneous medium has the same properties at every point; it is uniform without irregularities.

[2] An isotropic medium is one such that the permittivity, ϵ, and permeability, μ, of the medium are uniform in all directions of the medium, the simplest instance being free space.

[3] Low frequency is the International Telecommunication Union (ITU) definition for radio frequency in the range of $30kHz - 300kHz$.

Then it is possible to define the relation between *permittivity* ϵ and *permeability* μ with the *electric* and *magnetic susceptibilities* of the material as follows:

$$\begin{aligned} \epsilon &= \epsilon_0(1+\chi) \\ \mu &= \mu_0(1+\chi_m) \end{aligned} \tag{2.9}$$

Electric and magnetic susceptibilities are measures of material's polarization. Inserting Equation (2.9) in (2.8) the costitutive relations become:

$$\mathbf{D} = \epsilon_0\mathbf{E} + \mathbf{P} \qquad \mathbf{B} \ = \mu\mathbf{H} \tag{2.10}$$

where the vector **P** represents the *dielectric polarization* of the material and **M** represents the *magnetization*.

Finally, the *speed of the light* and the *characteristic impedance* in the medium are:

$$c = \frac{1}{\sqrt{\mu\epsilon}} \qquad \eta \ = \sqrt{\frac{\mu}{\epsilon}} \tag{2.11}$$

2.1.3 Equation of Propagation

The equation of propagation is given by replacing Equations (2.1) and (2.10) into the following vectorial equation:

$$\boldsymbol{\nabla} \times [\boldsymbol{\nabla} \times \mathbf{E}] = \boldsymbol{\nabla}[\boldsymbol{\nabla} \cdot \mathbf{E}] - \nabla^2\mathbf{E} \tag{2.12}$$

The l.h.s is the combination of Faraday's, Ampére's law and the constitutive relations (2.8), therefore can be written as:

$$\boldsymbol{\nabla} \times [\boldsymbol{\nabla} \times \mathbf{E}] = -\mu\epsilon\frac{\partial\mathbf{E}^2}{\partial t^2} - \mu\frac{\partial\mathbf{J}}{\partial t} \tag{2.13}$$

The r.h.s using the Gauss's law $\boldsymbol{\nabla} \cdot \mathbf{D} = \rho$, can be written as:

$$\boldsymbol{\nabla}[\boldsymbol{\nabla} \cdot \mathbf{E}] - \nabla^2\mathbf{E} = \frac{1}{\epsilon}\frac{\partial\boldsymbol{\nabla}\rho}{\partial t} - \nabla^2\mathbf{E} \tag{2.14}$$

Equating (2.13) with (2.14) and using the *Ohm's law*, $\mathbf{J} = \sigma\mathbf{E}$, the propagation's equation is obtained:

$$\nabla^2\mathbf{E} - \mu\epsilon\frac{\partial\mathbf{E}^2}{\partial t^2} - \mu\sigma\frac{\partial\mathbf{E}}{\partial t} = -\frac{1}{\epsilon}\frac{\partial\boldsymbol{\nabla}\rho}{\partial t} \tag{2.15}$$

2.1.4 Plane Waves

Behind the hypothesis of *constant amplitude monochromatic plane wave* (which means *free of mobile electric charges*, *homogenous* and *lossless* medium), the r.h.s of Equation (2.15) is null, defining in this way the *d'Alembert's Equation*:

$$\nabla^2\mathbf{E} - \mu\epsilon\frac{\partial\mathbf{E}^2}{\partial t^2} = 0 \tag{2.16}$$

It may be simplified considering a complex version of the monochromatic time-space electric field analyzed under radial reference system. Therefore, the harmonic solution in time domain is:

$$\mathbf{E}(\mathbf{r}, t) = \Re\left[\mathbf{E}(\mathbf{r})e^{jwt}\right] \tag{2.17}$$

The above complex vector $\mathbf{E}(\mathbf{r})$, represents a monochromatic plane wave. It can be rewritten, as all the complex vectors, using the phasor representation:

$$\mathbf{E}(\mathbf{r}) = \mathbf{E}_0 e^{-j\mathbf{kr}} \tag{2.18}$$

where $\mathbf{k}$ is called *wave vector* and indicates the *propagation direction*. The electric complex vector has to be orthogonal to the wave propagation direction, therefore the relation $\mathbf{E}(\mathbf{r}) \cdot \hat{\mathbf{k}} = 0$ has to be verified.

In a orthogonal basis system $\hat{x}, \hat{y}, \hat{z}$, defining the propagation's direction as $\hat{\mathbf{k}} = \hat{z}$, the electric field expression is:

$$\mathbf{E}(\mathbf{r}) = \mathbf{E}_0 e^{-\alpha z} e^{-j\beta z}, \qquad E_{0z} = 0 \tag{2.19}$$

where α is the attenuation factor, while β has the same function of the wave number in the time domain. Introducing the Equation (2.19) in Equation (2.17), an easier expression of electric field is founded:

$$\mathbf{E}(z,t) = \Re\left[\mathbf{E}_0 e^{-\alpha z} e^{-j\beta z} e^{jwt}\right] \tag{2.20}$$

with a representation component by component and simplifying the factor α, the explicit expression of Equation (2.20) becomes:

$$\mathbf{E}(z,t) = \begin{bmatrix} E_{0x} cos(\omega t - kz + \delta_x) \\ E_{0y} cos(\omega t - kz + \delta_y) \\ 0 \end{bmatrix} \tag{2.21}$$

Fixing the time as $t = t_0$, the obtained electric field as shown in Figure 2.1[4], is composed of two sinusoidal waves which are orthogonal each other and with, in general, different amplitudes and phases at the origin [5].

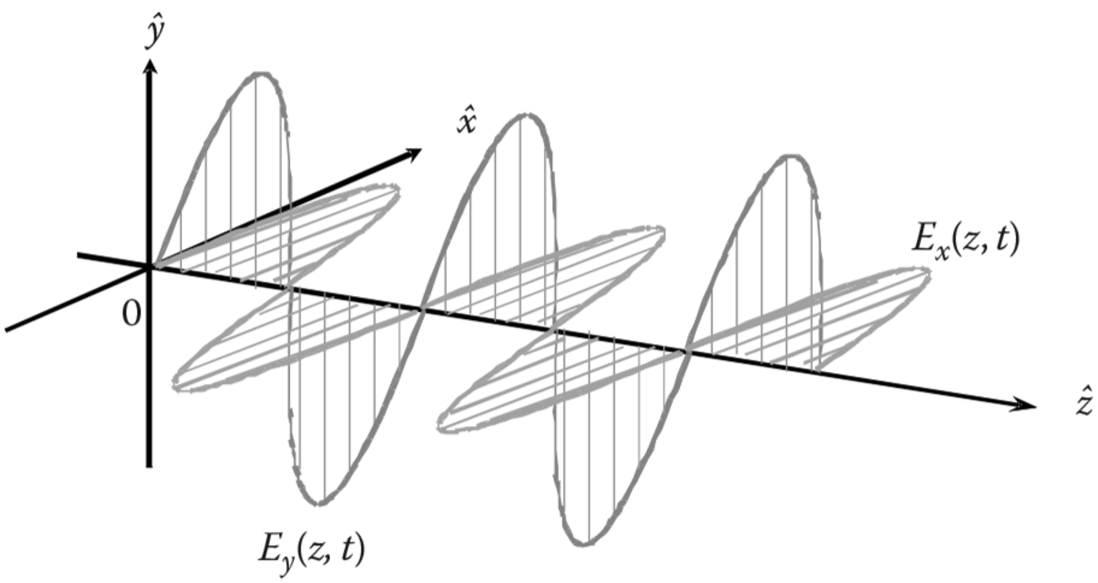

Figure 2.1: Spatial evolution of monochromatic plane wave components.

[4] Image taken from [5].

Editing Equation (2.21), three main polarization are implementable:

- *Linear Polarization*[5]: $\delta = \delta_y - \delta_x = 0$.

$$\mathbf{E}(z_0, t) = \sqrt{E_{0x}^2 + E_{0y}^2} \begin{bmatrix} \cos\phi \\ \sin\phi \\ 0 \end{bmatrix} \cos(\omega t_0 - kz + \delta_x) \tag{2.22}$$

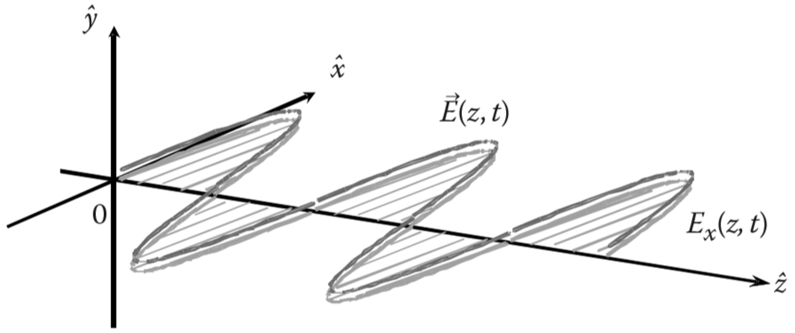

Figure 2.2: Spatial evolution of a linearly polarized plane wave.

- *Circular Polarization*[6]: $\delta = \delta_y - \delta_x = \frac{\pi}{2} + k\pi$ and $E_{0x} = E_{0y}$.

  Wave rotates around the $\hat{z}$ axis with constant modules and orientation given by the angle $\phi(z)$:

$$\left|\mathbf{E}(z, t_0)\right|^2 = E_{0x}^2 + E_{0y}^2, \qquad \phi(z) = \pm(\omega t_0 - kz + \delta_x) \tag{2.23}$$

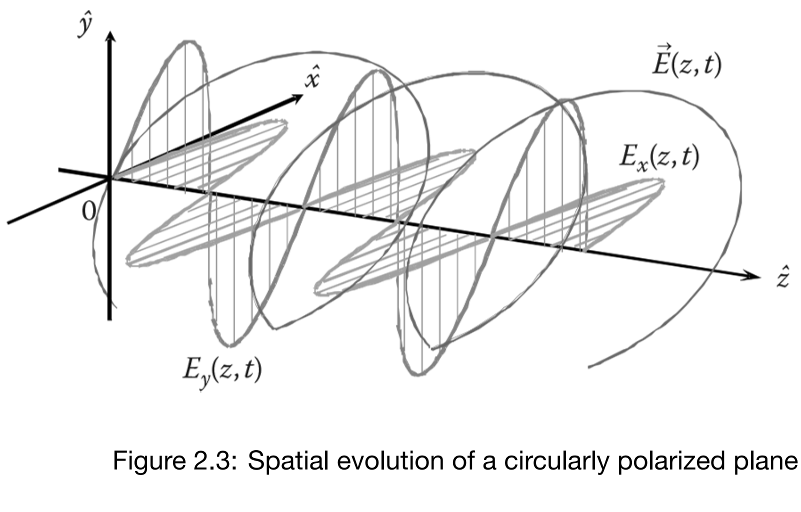

Figure 2.3: Spatial evolution of a circularly polarized plane wave.

[5] Image taken from [5].
[6] Image taken from [5].

- *Elliptic Polarization*[7]:

  In this case are stored all the other possible polarizations, where the wave makes helical trajectory around the $\hat{z}$ axis.

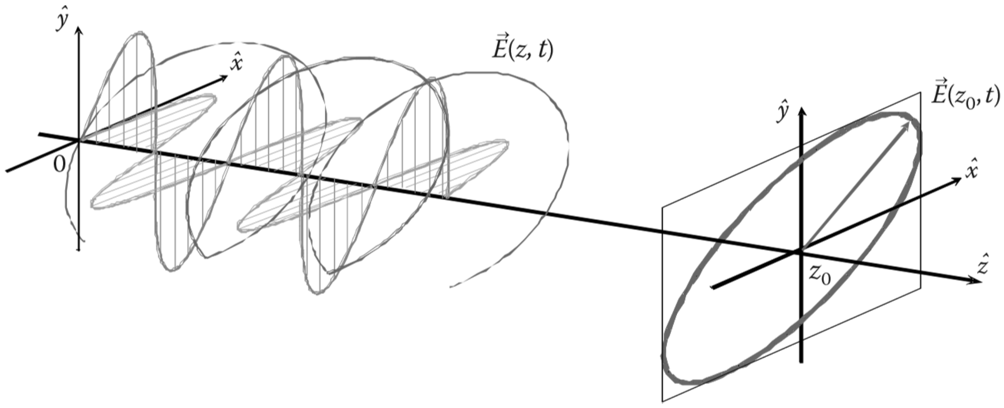

Figure 2.4: Spatial evolution of a elliptically polarized plane wave.

2.1.5 Elliptical Polarization

The analyse about the elliptical polarization is done fixing the electromagnetic field in a plan $z = z_0$, which is transverse to the propagation direction $\hat{z}$. Drawing the time variation of the electric vector, on a fixed plane, generates an elliptical curve as shown in Figure 2.5[8]:

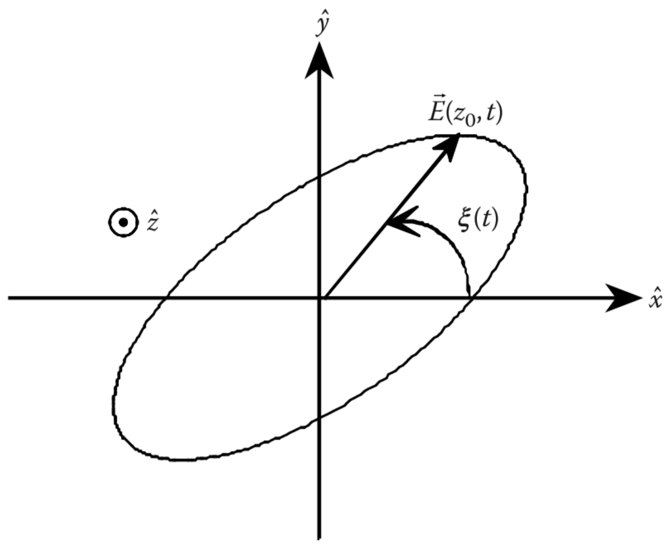

Figure 2.5: Electromagnetic vector time domain rotation.

[7] Image taken from [5].
[8] Image taken from [5].

Thus, the trajectory is determined from a parametric complicated version of a well-known *ellipse equation*:

$$\left[\frac{E_x(z_0,t)}{E_0x}\right]^2 - 2\frac{E_x(z_0,t)E_y(z_0,t)}{E_{0x}E_{0y}}\cos(\delta_y-\delta_x) + \left[\frac{E_y(z_0,t)}{E_0y}\right]^2 = \sin(\delta_y-\delta_x) \quad (2.24)$$

Otherwise, the ellipse shape is characterized using three parameters:

- *Ellipse Amplitude*:

$$A = \sqrt{E_{0x}^2 + E_{0y}^2} \quad (2.25)$$

- *Ellipse Orientation*: is the angle among the ellipse major axis and $\hat{x}$ axis.

$$\tan(2\phi) = 2\frac{E_{0x}E_{0y}}{E_{0x}^2 - E_{0y}^2}\cos(\delta), \qquad \psi \in \left[-\frac{\pi}{2}, \frac{\pi}{2}\right] \quad (2.26)$$

  where $\delta = \delta_y - \delta_x$.

- *Ellipticity*:

$$|\sin(2\tau)| = 2\frac{E_{0x}E_{0y}}{E_{0x}^2 - E_{0y}^2}\sin(\delta)|, \qquad |\tau| \in \left[0, \frac{\pi}{4}\right] \quad (2.27)$$

Ellipse amplitude, *ellipse orientation* and *ellipticity* are illustrated in Figure 2.6[9].

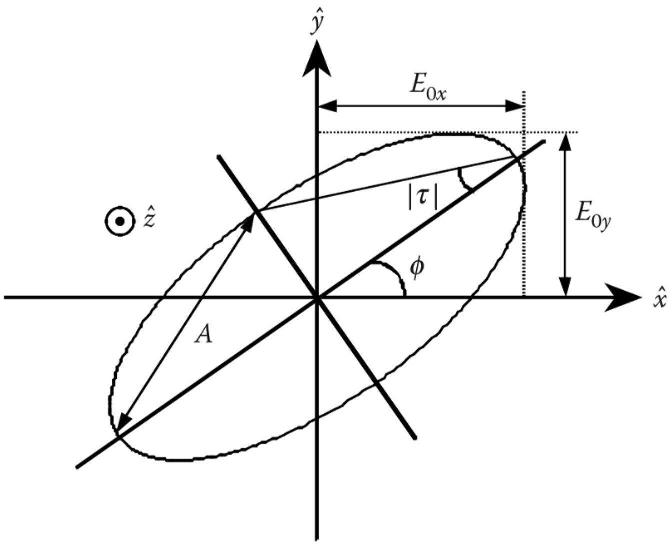

Figure 2.6: Polarization ellipse.

[9]Image taken from [5].

2.2 Synthetic Aperture Radar

In *Remote Sensing* the image acquisition is made using a special instruments called *Synthetic Aperture Radar* (SAR) [9]. It may be described as a radar mounted on an airborne or spaceborne system which uses the platform path to increase the aperture of the radar antenna. This method allows to focus the directivity antenna in a larger area, generating high-resolution remote sensing images. SAR can be seen as a unique antenna that transmits pulses and receives their echoes, at the same time it is moving [10]. This kind of acquisition realizes an array of value which are obtained in different position. It is called *Synthetic Array*. The main reason about the use of SAR system in Remote Sensing are three [5]:

- SAR is an active system, so it can work in darkness and unfavourable meteorological conditions.
- SAR can work in microwave frequencies, then the clouds and precipitations are almost completely invisible for the radar.
- SAR are competitive with and complementary to multispectral radiometers as the primary remote sensing instruments.

A SAR system, flying over an area, transmits phase-encoded pulses and receives the echoes reflected from the earth's surface, aiming the radar beam approximately perpendicular to the flight direction. This is the *monostatic* case, where the transmit and receive antennas are the same, otherwise the *bistatic* expected two different antennas, which are separated by a distance that is comparable to the expected target distance.

The intensity image is developed along the two directions illuminated by the radar beam as shown in Figure 2.7[10]. The first direction follows the flight direction and it is called *Along-Track Direction* (axis $\hat{y}$). The second is orthogonal to the flight direction and it is called *Across-Track Direction* (axis $\hat{x}$); in this case, the time delay of the received echo, is proportional to the distance from the sensor.

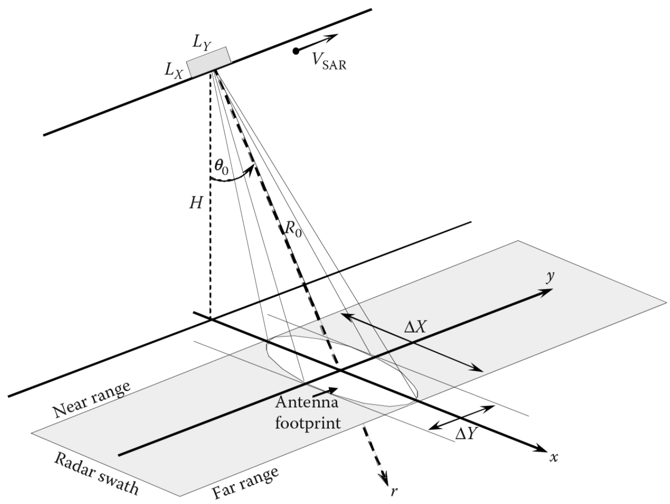

Figure 2.7: SAR geometry for a side-looking radar system.

[10] Image taken from [5].

Before discussing the SAR *resolution*, it is necessary to introduce some terms of radar imaging. Let us take a transverse view, about the previous side-looking, fixing the plane $y = y_0$. Referring to Figure 2.8 [11]:

- *Look Angle*: refers to the angle between the vertical direction and the radar beam at the radar platform.
- *Incidence Angle*: refers to the angle between the vertical direction and the radar wave propagation vector at the surface.
- *Depression Angle*: refers to the angle between the radar beam and the horizontal at the radar platform.
- *Grazing Angle*: refers to the angle between the horizontal at the surface and the incident wave.
- *Slant Range*: refers to the range along the radar line-of-sight.
- *Ground Range*: refers to the range along a smooth surface (the ground) to the scatterer.

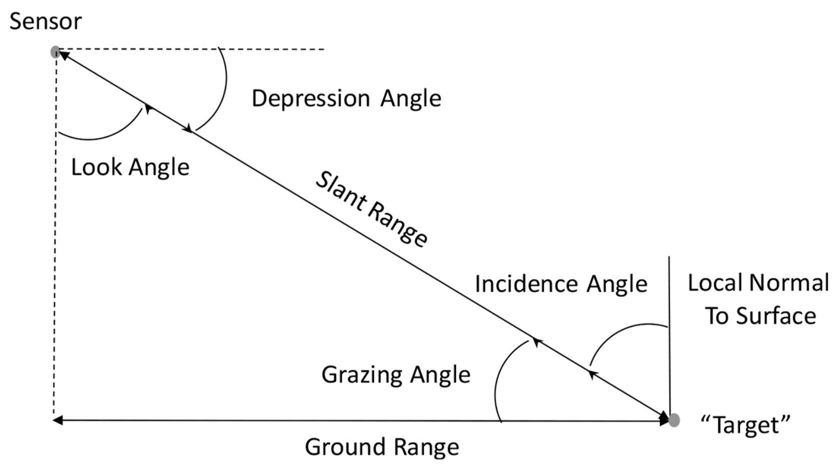

Figure 2.8: SAR geometry for a transverse side-looking sensor.

The slant range resolution is given by:

$$\delta_r = \frac{c}{2B} \tag{2.28}$$

where c is the speed of light and B is the bandwidth of the transmitted signal.

The ground range resolution is equal to half of the antenna footprint on the surface, it means a change of resolution with a variation of incidence angle.

$$\delta_x = \frac{\delta_r}{\sin(\theta)} \tag{2.29}$$

where θ is the look angle.

[11] Image taken from [11].

2.3 Polarimetric Synthetic Aperture Radar

Section 2.1 presents how the electromagnetic wave passes through the medium and which are the ways to represent it. Section 2.2, presents the SAR system, which uses a beam of electromagnetic waves for scanning the earth's surface, to get back information from it. When the incident wave hits the target, part of its energy is absorbed by the target itself, conversely all the unabsorbed energy is radiated again in the surrounding area as a new electromagnetic wave [5].

To characterize the target, using electromagnetic waves, two parameters may be used:

- *Radar Cross Section* (RCS): the target dimension is smaller than the footprint of the radar system. This configuration is called *Point Target*.
- *Normalized Radar Cross Section* (NRCS): the target dimension is larger than the footprint of the radar system. This configuration is called *Distributed Target*.

Target Point For defining this parameter it is necessary introduce the law that relates the *transmitted power* and the *received power* in a radar system. It is well-know as *Radar Equation* [12]:

$$P_R = \frac{P_T G_T(\theta,\phi)}{4\pi r_T^2}\sigma\frac{A_{eff}(\theta,\phi)}{4\pi r_R^2} \tag{2.30}$$

where P_R is the scattered power from the target and received by the radar system, P_T is the power transmitted by the radar system, G_T is the transmitting antenna gain, A_{eff} is the effective aperture area of the receiving antenna, r_T and r_R are the distance *transmitting-system/target* and *target/receiving-system* respectively, θ and ϕ are the angle used for defining the transmission and reception direction, finally σ is the previously introduced RCS. The RCS is defined as the cross section of an equivalent idealized isotropic scatterer that generates the same scattered power density as the object in the observed direction [5]. The radar cross section is thus given by:

$$\sigma = 4\pi r^2 \frac{\left|\mathbf{E}_S\right|^2}{\left|\mathbf{E}_I\right|^2} \tag{2.31}$$

It is dependent of: *wave frequency* f, *wave polarization*, *incident direction* and *scattering direction*, *object geometrical structure* and *object dielectric structure*.

Distributed Target The target shall be seen as a infinite collection of statistically identical point targets. Equation (2.30), integrating over the area A_0 scanned by the beam, becomes:

$$P_R = \iint_{A_0} \frac{P_T G_T(\theta,\phi)}{4\pi r_T^2}\sigma^0\frac{A_{eff}(\theta,\phi)}{4\pi r_R^2}ds \tag{2.32}$$

All the parameters are the same as in the previous case except σ^0 that now is called NRCS and is made as a ratio of the statistically averaged scattered power density to the average incident power density over the surface of the sphere of radius r [5]:

$$\sigma^0 = \frac{\langle\sigma\rangle}{A_0} = \frac{4\pi r^2}{A_0}\frac{\left\langle\left|\mathbf{E}_S\right|^2\right\rangle}{\left|\mathbf{E}_I\right|^2} \tag{2.33}$$

where σ^0 is dimensionless.

2.3.1 Scattering Matrix

As shown in Section 2.1.4, an electric wave has a own polarization. Therefore let us define p as a generic polarization of the incident wave and q as a generic polarization of the scattered wave. RCS and NRCS can be rewritten as such:

$$\sigma_{qp} = 4\pi r^2 \frac{\left|\mathbf{E}_{S_q}\right|^2}{\left|\mathbf{E}_{I_p}\right|^2} \quad \text{and} \quad \sigma^0_{pq} = \frac{\langle \sigma_{qp} \rangle}{A_0} = \frac{4\pi r^2}{A_0} \frac{\left\langle \left|\mathbf{E}_{S_q}\right|^2 \right\rangle}{\left|\mathbf{E}_{I_p}\right|^2} \tag{2.34}$$

The polarization of a *plane, monochromatic, electric field* may be represented with the so-called Jones Vector. Moreover, two orthogonal Jones vectors may build a polarization base that is able to define all the possible polarization states about a given electromagnetic wave. All the interactions among the SAR system and the Earth's surface can be described as:

$$\mathbf{E}_S = \frac{e^{-jkr}}{r} [\mathbf{S}]\, \mathbf{E}_I = \frac{e^{-jkr}}{r} \begin{bmatrix} S_{pp} & S_{pq} \\ S_{qp} & S_{qq} \end{bmatrix} \mathbf{E}_I \tag{2.35}$$

Here, $\mathbf{E}_I$ and $\mathbf{E}_S$ are the Jones vectors of incident and scattered field. **S** is the *scattering matrix* while its element S_{ij} are called *complex scattering coefficient*. Diagonal elements are known as *co-polar*, contrariwise *off-diagonal* elements are known as *cross-polar*. The multiplicative factor e^{jkr}/r is the well-known *Green function* that describes the propagation for spherical waves.

The ratio of scattered and incident electromagnetic field from Equation (2.35) is:

$$\frac{\mathbf{E}_S}{\mathbf{E}_I} = \frac{e^{-jkr}}{r} \begin{bmatrix} S_{pp} & S_{pq} \\ S_{qp} & S_{qq} \end{bmatrix} \tag{2.36}$$

Then, combining Equation (2.34) and (2.36), the RCS may be rewritten as:

$$\sigma_{qp} = 4\pi \left|S_{qp}\right|^2 \tag{2.37}$$

Usually, the scattering matrix and the matrices that will be defined later use polarization directions which are parallel to unit vector of a Cartesian system $(\hat{x}, \hat{y})$. For simplicity let us define the *horizontal polarization* as $\hat{x} = \hat{u}_H$ and the *vertical polarization* as $\hat{y} = \hat{u}_V$.

A new form of scattering matrix can than be written:

$$\mathbf{S} = \begin{bmatrix} S_{HH} & S_{HV} \\ S_{VH} & S_{VV} \end{bmatrix} \tag{2.38}$$

All these concepts can be seen as a SAR system that transmits waves with horizontal and vertical polarization in two different moment. Subsequently it receives the scattered wave in each possible combination. That means four captured images, one for each channel: HH, HV, VH and VV. *Polarimetric Synthetic Aperture Radar* (PolSAR) is then called multi-channel SAR.

Before continuing with the analysis of the scattering process, it is necessary to briefly introduce the two most used coordinate systems in radar polarimetry. In both of the conventions, the coordinate system of incident and scattered waves are centred on the transmitting and receiving antennas, respectively. The two coordinate systems are called *Forward Scatter Alignment* (FSA) and *Backscatter Alignment* (BSA). The scattering matrices of both cases are related as:

$$\mathbf{S}_{BSA} = \begin{bmatrix} -1 & 0 \\ 0 & 1 \end{bmatrix} \mathbf{S}_{FSA} \tag{2.39}$$

2.3.2 Coherency and Covariance Matrices

The physical information extraction from the scattering matrix **S** is made through a vectorization operator on the matrix itself [5].

$$\mathbf{s} = \mathbf{V}(\mathbf{S}) = \frac{1}{2}\,\mathrm{Tr}\,(\mathbf{S}\mathbf{\Psi}) \tag{2.40}$$

Here, $\mathbf{\Psi}$ is a set of complex orthogonal basis matrices and $\mathrm{Tr}\,(\cdot)$ represent the *trace operator*.

Bistatic Scattering Case The term *bistatic scattering* is used when the system is composed of one transmitting antenna and one receiving antenna in two different positions.

The first set of matrices is the *complex Pauli spin matrix basis set*:

$$\{\Psi_P\} = \left\{ \sqrt{2}\begin{bmatrix}1 & 0\\ 0 & 1\end{bmatrix} \sqrt{2}\begin{bmatrix}1 & 0\\ 0 & -1\end{bmatrix} \sqrt{2}\begin{bmatrix}0 & 1\\ 1 & 0\end{bmatrix} \sqrt{2}\begin{bmatrix}0 & -j\\ j & 0\end{bmatrix} \right\} \tag{2.41}$$

The corresponding *4-D Pauli vector* becomes:

$$\mathbf{s} \triangleq \mathbf{k} = \frac{1}{\sqrt{2}}\begin{bmatrix}S_{HH}+S_{VV} & S_{HH}-S_{VV} & S_{HV}+S_{VH} & j(S_{XV}-S_{VH})\end{bmatrix}^T \tag{2.42}$$

The second set of matrices is the *complex Lexicographic spin matrix basis set*:

$$\{\Psi_L\} = \left\{ 2\begin{bmatrix}1 & 0\\ 0 & 0\end{bmatrix} 2\begin{bmatrix}0 & 1\\ 0 & 0\end{bmatrix} 2\begin{bmatrix}0 & 0\\ 1 & 0\end{bmatrix} 2\begin{bmatrix}0 & 0\\ 0 & 1\end{bmatrix} \right\} \tag{2.43}$$

The corresponding *4-D Lexicographic vector* becomes:

$$\mathbf{s} \triangleq \mathbf{\Omega} = \begin{bmatrix}S_{HH} & S_{HV} & S_{VH} & S_{VV})\end{bmatrix}^T \tag{2.44}$$

The total received power from the radar is called *Span* and is defined as:

$$\mathrm{Span}(\mathbf{S}) = \mathrm{Tr}\,(\mathbf{S}\mathbf{S}^H) = |S_{HH}|^2 + |S_{HV}|^2 + |S_{VH}|^2 + |S_{VV}|^2 = |\mathbf{k}|^2 = |\mathbf{\Omega}|^2 \tag{2.45}$$

The scattered wave, behind the hypothesis of the distributed target, usually has a partially polarized plane wave state, which is described by the complex correlations of the electric field components [13]. Let us define two matrices able to take in account the correlation between the electric field transmitted and received.

4×4 *Polarimetric Coherency*[12] matrix **T** derived from the target vector **k**:

$$\mathbf{T} = \langle \mathbf{k}\mathbf{k}^H \rangle \tag{2.46}$$

4×4 *Polarimetric Covariance* matrix **C** derived from the target vector $\mathbf{\Omega}$:

$$\mathbf{C} = \langle \mathbf{\Omega}\mathbf{\Omega}^H \rangle = \tag{2.47}$$

$$= \begin{bmatrix}
\langle |S_{HH}|^2 \rangle & \langle S_{HH}S_{HV}^* \rangle & \langle S_{HH}S_{VH}^* \rangle & \langle S_{HH}S_{VV}^* \rangle \\
\langle S_{HV}S_{HH}^* \rangle & \langle |S_{HV}|^2 \rangle & \langle S_{HV}S_{VH}^* \rangle & \langle S_{HV}S_{VV}^* \rangle \\
\langle S_{VH}S_{HH}^* \rangle & \langle S_{VH}S_{HV}^* \rangle & \langle |S_{VH}|^2 \rangle & \langle S_{VH}S_{VV}^* \rangle \\
\langle S_{VV}S_{HH}^* \rangle & \langle S_{VV}S_{HV}^* \rangle & \langle S_{VV}S_{VH}^* \rangle & \langle |S_{VV}|^2 \rangle
\end{bmatrix}$$

[12]The complete representation of the 4×4 Polarimetric Coherency matrix is shown in Appendix.

Monostatic Scattering Case The term *monostatic scattering* is used when the system is composed of a unique antenna which is able to transmit and receive.

The first set of matrices used for the vectorization of **S** is the *complex Pauli spin matrix basis set*:

$$\{\Psi_P\} = \left\{ \sqrt{2}\begin{bmatrix}1 & 0\\0 & 1\end{bmatrix} \sqrt{2}\begin{bmatrix}1 & 0\\0 & -1\end{bmatrix} \sqrt{2}\begin{bmatrix}0 & 1\\1 & 0\end{bmatrix} \right\} \tag{2.48}$$

The corresponding *3-D Pauli vector* becomes:

$$\mathbf{s} \triangleq \mathbf{k} = \frac{1}{\sqrt{2}}\begin{bmatrix}S_{HH}+S_{VV} & S_{HH}-S_{VV} & 2S_{HV}\end{bmatrix}^T \tag{2.49}$$

The second set of matrices used for the vectorization of **S** is the *complex Lexicographic spin matrix basis set*:

$$\{\Psi_L\} = \left\{ 2\begin{bmatrix}1 & 0\\0 & 0\end{bmatrix} 2\sqrt{2}\begin{bmatrix}0 & 1\\0 & 0\end{bmatrix} 2\begin{bmatrix}0 & 0\\0 & 1\end{bmatrix} \right\} \tag{2.50}$$

The corresponding *3-D Lexicographic vector* becomes:

$$\mathbf{s} \triangleq \mathbf{\Omega} = \begin{bmatrix}S_{HH} & \sqrt{2}S_{HV} & S_{VV})\end{bmatrix}^T \tag{2.51}$$

The total received power from the radar is:

$$\text{Span}(\mathbf{S}) = \text{Tr}\left(\mathbf{SS}^H\right) = \left|S_{HH}\right|^2 + 2\left|S_{HV}\right|^2 + \left|S_{VV}\right|^2 = \left|\mathbf{k}\right|^2 = \left|\mathbf{\Omega}\right|^2 \tag{2.52}$$

As for the bistatic scattering case, let us define two matrices able to take into account the correlation between the transmitted and received electric fields.

3×3 *Polarimetric Coherency* matrix **T** derived from the target vector **k**:

$$\mathbf{T} = \langle \mathbf{k} \cdot \mathbf{k}^H \rangle = \tag{2.53}$$

$$= \frac{1}{2}\begin{bmatrix} \left\langle |S_{HH}+S_{VV}|^2 \right\rangle & \left\langle (S_{HH}+S_{VV})(S_{HH}-S_{VV})^* \right\rangle & 2\left\langle (S_{HH}+S_{VV})S_{HV}^* \right\rangle \\ \left\langle (S_{HH}-S_{VV})(S_{HH}+S_{VV})^* \right\rangle & \left\langle |S_{HH}-S_{VV}|^2 \right\rangle & 2\left\langle (S_{HH}-S_{VV})S_{HV}^* \right\rangle \\ 2\left\langle S_{HV}(S_{HH}+S_{VV})^* \right\rangle & 2\left\langle S_{HV}(S_{HH}-S_{VV})^* \right\rangle & 4\left\langle |S_{HV}|^2 \right\rangle \end{bmatrix}$$

3×3 *Polarimetric Covariance* matrix **C** derived from the target vector $\mathbf{\Omega}$:

$$\mathbf{C} = \langle \mathbf{\Omega} \cdot \mathbf{\Omega}^H \rangle = \tag{2.54}$$

$$= \begin{bmatrix} \left\langle |S_{HH}|^2 \right\rangle & \sqrt{2}\left\langle S_{HH}S_{HV}^* \right\rangle & \left\langle S_{HH}S_{VV}^* \right\rangle \\ \sqrt{2}\left\langle S_{HV}S_{HH}^* \right\rangle & 2\left\langle |S_{HV}|^2 \right\rangle & \sqrt{2}\left\langle S_{HV}S_{VV}^* \right\rangle \\ \left\langle S_{VV}S_{HH}^* \right\rangle & \sqrt{2}\left\langle S_{VV}S_{HV}^* \right\rangle & \left\langle |S_{VV}|^2 \right\rangle \end{bmatrix}$$

In both the bistatic and monostatic cases, the operator $\langle \cdot \rangle$ was used, that may represent the temporal or spatial ensemble averaging, defined as:

- Temporal averaging:

$$\langle s(t) \rangle = \lim_{T \to \infty} \frac{1}{T} \int_0^T s(t)dt \tag{2.55}$$

- Spatial averaging:

$$\langle s \rangle = \frac{1}{L} \sum_{i=1}^{L} s_i \tag{2.56}$$

2.3.3 Polarimetric Decomposition

First of all it is necessary split the *decomposition* topic in two big cases:

- *Coherent Decomposition*:

  The main task of the coherent decomposition is to show the scattering matrix **S**, acquired by radar, as combination of the scattering responses of *simpler objects*:

$$\mathbf{S} = \sum_{i}^{k} c_i \mathbf{S}_i \tag{2.57}$$

  where $\mathbf{S}_i$ represents the scattering response of each simpler object, instead c_i is the weight that the respective scattering response in the total scattering process.

  The scattering matrix may feature the peculiar process of a given target or the target itself. That happens only in completely polarized case of the incident and scattered wave. Accordingly, coherent target decomposition is applicable only to coherent target, or in other words, to the *point target*.

- *Incoherent Decomposition*:

  Conversely, **S** cannot feature, in a planimetric way, the *distributed target*. Due about speckle, they are statistically characterized only. Since speckle noise must be reduced, only second order polarimetric representations can be employed to analyze distributed scatterers [14]. These second order descriptors are the **T** and **C** matrices shown in Section 2.3.2. The task of the incoherent decomposition is to write the two matrices as a combination of second order descriptors to simpler object, which have a easier physical interpretation. The decomposition can then be expressed as:

$$\begin{aligned} \mathbf{T} &= \sum_{i}^{k} q_i \mathbf{T}_i \\ \mathbf{C} &= \sum_{i}^{k} p_i \mathbf{C}_i \end{aligned} \tag{2.58}$$

  where $\mathbf{T}_i$ and $\mathbf{C}_i$ represent the scattering response of each simpler object. Instead p_i and q_i are the respectively weight.

In the following work has been uses a specific kind of incoherent decomposition well-known as $H/A/\bar{\alpha}$ *Polarimetric Decomposition*, which use a smoothing algorithm based on second-order statistic [5]. An important thing to mark is that this technique does not fix a specific statistical distribution hypothesis.

The following handling has been made bearing in mind that is possible to pass from **C** to **T** through the relation:

$$\mathbf{T} = \mathbf{U}\mathbf{C}\mathbf{U}^{-1} \tag{2.59}$$

where **U** is called *special unitary transformation* and it is equal to:

$$\mathbf{U} = \frac{1}{\sqrt{2}} \begin{bmatrix} 1 & 0 & 1 \\ 1 & 0 & -1 \\ 0 & \sqrt{2} & 0 \end{bmatrix} \tag{2.60}$$

Therefore the coherency matrix **T** is analyzed behind the concepts of *eigenvectors* and their relative *eigenvalues*, where is supposed a dominant average scattering mechanism in each cell. *The task of this decomposition is to discover which one is the dominant mechanism for each cell*.

The coherency matrix is then written as:

$$\mathbf{T} = \mathbf{V}\boldsymbol{\Lambda}\mathbf{V}^{-1} = \mathbf{V}\begin{bmatrix}\lambda_1 & 0 & 0\\ 0 & \lambda_2 & 0\\ 0 & 0 & \lambda_3\end{bmatrix}\mathbf{V}^{-1} \tag{2.61}$$

It is known as *diagonal form* and it is able to physically show the statistically independence between a set of target vectors. $\boldsymbol{\Lambda}$ is a 3×3 diagonal matrix composed by nonnegative real elements called eigenvalues, while $\mathbf{V} = \begin{bmatrix}\mathbf{v}_1 & \mathbf{v}_2 & \mathbf{v}_3\end{bmatrix}$ is a 3×3 unitary matrix, whose three element are the unit orthogonal eigenvectors. Assuming scattering medium and absence of azimuth symmetry [15], each eigenvector of **T** gets the form:

$$\mathbf{v} = \begin{bmatrix}\cos(\alpha)e^{j\phi} & \sin(\alpha)\cos(\beta)e^{j(\delta+\phi)} & \sin(\alpha)\sin(\beta)e^{j(\gamma+\phi)}\end{bmatrix}^T \tag{2.62}$$

Then, each column of the full version of **V** represents an orthogonal eigenvector [16]:

$$\mathbf{V} = \begin{bmatrix}\cos(\alpha_1)e^{j\phi_1} & \cos(\alpha_2)e^{j\phi_2} & \cos(\alpha_3)e^{j\phi_3}\\ \sin(\alpha_1)\cos(\beta_1)e^{j(\delta_1+\phi_1)} & \sin(\alpha_2)\cos(\beta_2)e^{j(\delta_2+\phi_2)} & \sin(\alpha_3)\cos(\beta_3)e^{j(\delta_3+\phi_3)}\\ \sin(\alpha_1)\sin(\beta_1)e^{j(\gamma_1+\phi_1)} & \sin(\alpha_2)\sin(\beta_2)e^{j(\gamma_2+\phi_2)} & \sin(\alpha_3)\sin(\beta_3)e^{j(\gamma_3+\phi_3)}\end{bmatrix}$$

The column vectors form is the same, but their parameters $\alpha, \beta, \delta, \gamma$ and ϕ are different, it can be thought as an probabilistic interpretation of the scattering process. Moreover, the columns are mutually orthogonal, thus every parameter is not independent from the same parameter in the other vector. In other words, taking for example into account the first parameter α, the mutually orthogonal property means α_1, α_2 and α_3 are not independent each other.

$\bar{\alpha}$ parameter The statistical scatterer model is saw as a Bernoulli process of 3 variables. The target is model as a sum of three **S** matrices represented by the columns of the 3×3 unitary **V** matrix [5], which occurred with pseudo-probabilities P_i:

$$P_i = \frac{\lambda_i}{\left(\sum_{k=1}^{3}\lambda_k\right)}, \qquad \sum_{i=1}^{3} P_i = 1 \tag{2.63}$$

The generic target parameter α follows a random sequence as:

$$\alpha = \{\alpha_1\alpha_2\alpha_3\alpha_1\alpha_2\alpha_3\alpha_1\alpha_2\alpha_3\dots\} \tag{2.64}$$

therefore, the best parameter's estimation is given by the mean of the terms, where each one weighted with its pseudo-probability:

$$\bar{\alpha} = \sum_{i=1}^{3} P_i\alpha_i \tag{2.65}$$

The method used about α is repeated for all parameters:

$$\bar{\beta} = \sum_{i=1}^{3} P_i\beta_i \qquad \bar{\delta} = \sum_{i=1}^{3} P_i\delta_i \qquad \bar{\gamma} = \sum_{i=1}^{3} P_i\gamma_i \qquad \bar{\phi} = \sum_{i=1}^{3} P_i\phi_i \tag{2.66}$$

Being the matrix $\mathbf{\Lambda}$ made by the eigenvalues, which give the magnitude of the respectively eigenvectors, the mean target power, called Span, is defined as:

$$\bar{\lambda} = \sum_{i=1}^{3} P_i \lambda_i \tag{2.67}$$

Two extremes case may happen:

- Only one eigenvalue is nonzero: $\lambda_1 \neq 0, \lambda_2 = \lambda_3 = 0$.
- All eigenvalues are nonzero and identical: $\lambda_1 = \lambda_2 = \lambda_3 \neq 0$.

The parameters H and A are evaluable when λ does not belong at the previous two extremes cases, that is the case where distributed or partially polarized scatterers prevails.

***H* parameter** The *Entropy* H defines the degree of statistical disorder about each kind of scatterer. It may be seen as a measure of randomness in scattering mechanisms [17] and it is given by:

$$H = -\sum_{i=1}^{N} P_i \log_N(P_i) \tag{2.68}$$

Here, P_i is the pseudo-probability above defined, while the basis of the logarithmic function is $N = 3$ for the monostatic case and $N = 4$ for the bistatic case.

Low Entropy values $(H < 0.3)$ means weakly depolarizing system and than the dominant scattered component may be discovered (an example of low Entropy values is the ocean area). High Entropy values means depolarizing system and then a equivalent point scatter does not exist (an example of high Entropy values is the parkland area). If the Entropy reaches the value $H = 1$ the target scattering is truly a random noise process and the polarization information is zero [5]. Between the low and high case there are several mixture cases of low and high Entropy values (an example of mixture Entropy values is the urban area).

***A* parameter** An other parameter for describing the randomness of the scattering problem is the *Anisotropy* A, which measures the relative importance of the second and third eigenvalues of the decomposition. For define A is necessary to order the eigenvalues in the following way:

$$\lambda_1 > \lambda_2 > \lambda_3 > 0 \tag{2.69}$$

The Anisotropy is then given by:

$$A = \frac{\lambda_2 - \lambda_3}{\lambda_2 + \lambda_3} \tag{2.70}$$

Entropy H and Anisotropy A are complementary each other.

$H/\bar{\alpha}$ classification plane A further analysis about scattering mechanisms can be find out taking in account both H and $\bar{\alpha}$ parameters. H describes the amount of disorder given by scatters and $\bar{\alpha}$ is able to identify the average typology of scattering mechanisms from that area. Placing H and $\bar{\alpha}$ in a unique plane has been made a classification plane, which is characterized by nine basic zones with different scattering mechanisms behaviour.

The plan in question is shown in Figure 2.9 [13], where it has been divided the main behaviour of the possible scattering mechanism in: *double bounce scattering*, *volume diffusion* and *surface scattering*.

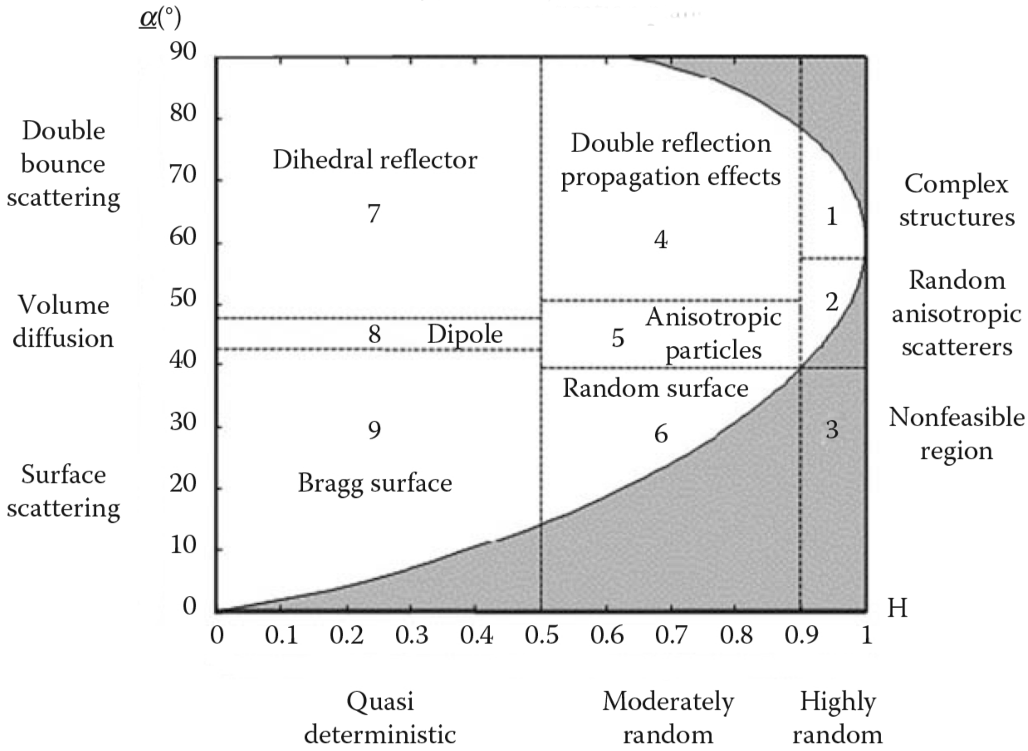

Figure 2.9: Classification plane.

A brief description of each zone is reported below:

- Zone 1: high entropy and multiple scattering.
- Zone 2: high entropy and vegetation scattering.
- Zone 3: high entropy and surface scatter.
- Zone 4: medium entropy and multiple scattering.
- Zone 5: medium entropy and vegetation scattering.
- Zone 6: medium entropy and surface scatter.
- Zone 7: low entropy and scattering events.
- Zone 8: low entropy and dipole scattering.
- Zone 9: low entropy and surface scatter.

[13] Image taken from [11].

2.4 Appendix

Polarimetric Coherency Matrix

$$\mathbf{T} = \frac{1}{2}\begin{bmatrix} \left\langle |S_{HH}+S_{VV}|^2 \right\rangle & \left\langle (S_{HH}+S_{VV})(S_{HH}-S_{VV})^* \right\rangle & \left\langle (S_{HH}+S_{VV})(S_{HV}+S_{VH})^* \right\rangle & \left\langle -j(S_{HH}+S_{VV})(S_{HV}-S_{VH})^* \right\rangle \\ \left\langle (S_{HH}-S_{VV})(S_{HH}+S_{VV})^* \right\rangle & \left\langle |S_{HH}-S_{VV}|^2 \right\rangle & \left\langle (S_{HH}-S_{VV})(S_{HV}+S_{VH})^* \right\rangle & \left\langle -j(S_{HH}-S_{VV})(S_{HV}-S_{VH})^* \right\rangle \\ \left\langle (S_{HV}+S_{VH})(S_{HH}+S_{VV})^* \right\rangle & \left\langle (S_{HV}+S_{VH})(S_{HH}-S_{VV})^* \right\rangle & \left\langle |S_{HV}+S_{VH}|^2 \right\rangle & \left\langle -j(S_{HV}+S_{VH})(S_{HV}-S_{VH})^* \right\rangle \\ \left\langle j(S_{HV}-S_{VH})(S_{HH}+S_{VV})^* \right\rangle & \left\langle j(S_{HV}-S_{VH})(S_{HH}-S_{VV})^* \right\rangle & \left\langle j(S_{HV}-S_{VH})(S_{HV}+S_{VH})^* \right\rangle & \left\langle |S_{HV}-S_{VH}|^2 \right\rangle \end{bmatrix}$$

Speckle 3

SAR images are affected by a granular disturbance pattern which is derived from the coherent interference of waves reflected from all the elementary scatterers present in the observed areas called *resolution cell* [18] [19]. The disturbance may not be considered as a simple noise, because it is tightly related to the SAR measurement principle. This phenomenon, called *Speckle*, technically is a pixel-to-pixel intensity variation [5]. The effect are to make the content of the analyzed image hard to understand, to reduce the effectiveness of target detection, image segmentation and classification.

The task of this thesis work is to find the best way to realize an easier and better performing method for information extraction using several tools as:

- Polarimetric parameter estimation.
- Spatial parameter estimation.
- Ground cover classification.
- Algorithms for speckling filtering.

For this reason it is necessary to figure out the SAR speckle statistics. First, we look at statistic for single channel ***SAR !*** (**SAR !**), about single-look and multi-look data. Then, we consider the multi channel SAR case. Both cases are treated considering the hypothesis of a homogenous surface, excluding the environment *texture* which is explained in Section 4.2.3.

3.1 The Physical Origin of Speckle

The radar beam hits limited area called resolution cell which presents surface variation compared to the radar wavelength. As shown in Figure 3.1[1], the surface appears as composed of many different elementary scatterers which, after the interaction with the SAR waves, radiates a backscattered wave with a changed amplitude and phase.

[1] Image taken from [5].

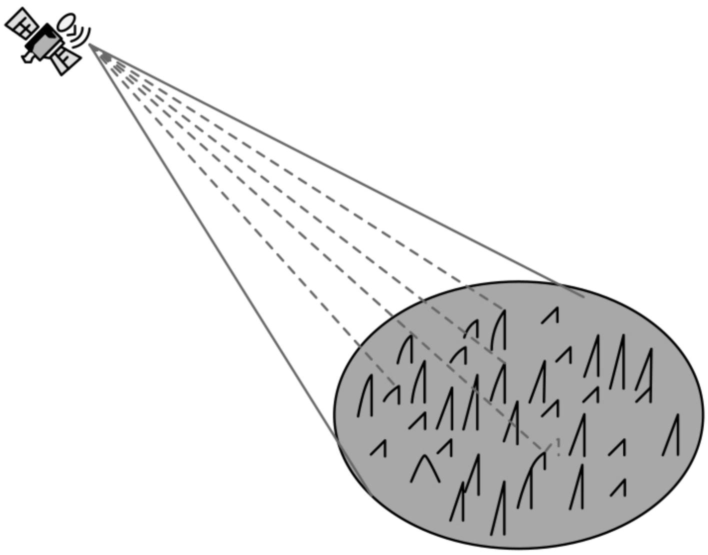

Figure 3.1: Radar beam on the resolution cell.

This causes the received signal to become the coherent sum (shown in Figure 3.2[2]) of all the backscattered waves radiated from a whole resolution cell. Coherent sum means that the amplitude and phase of each radiation vector is taken into account, therefore two limit cases may be occur:

- *Strong received signal*: if the coherent sum is made constructively (radiation vectors are closer in term of phase).
- *Weak received signal*: if the coherent sum is made destructively (radiation vectors are far in term of phase).

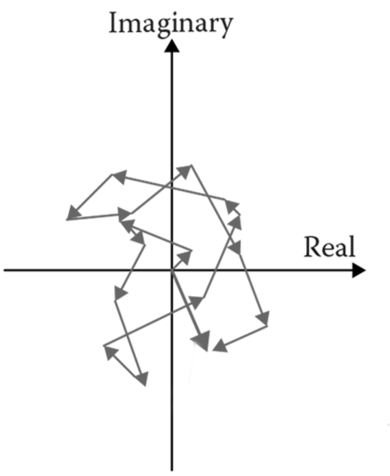

Figure 3.2: Coherent sum from the resolution cell terms.

[2] Image taken from [5].

The backscattered waves are complex vectors, so they can be expressed by *real* and *imaginary* components. Calling x the real component and y the imaginary component about the i-th vector, the coherent sum vector in cartesian coordinates is given by:

$$\mathbf{z} = x + jy = \sum_{i=1}^{n} x_i + j \sum_{i=1}^{n} y_i = \sum_{i=1}^{n} (x_i + jy_i) \tag{3.1}$$

Where n is the number of illuminated scatterers. It is unknown, but it must be large.

Switching to polar coordinates:

$$\mathbf{z} = Ae^{j\phi} = \sum_{i=1}^{n} A_i e^{j\phi_i} \tag{3.2}$$

The individual scattering amplitude A_i and phase ϕ_i are unobservable because the individual scatterers are on much smaller scales than the resolution of the SAR and normally there are many scatters per resolution cell. This behaviour might be interpreted as a *Random Walk Model* which causes a spatial variation of intensity making a granular pattern called *Speckle*.

3.2 Polarimetric SAR Speckle Statistics

The following discussion assumes four hypothesis:

- *Homogeneous medium*: it has the same properties at every point and it is uniform without irregularities.
- *Distributed target*: the resolution cell contains a large number of scatterers and no one of them has a reflected signal much stronger than the others [19].
- *Large range distance*: it is much larger than many radar wavelengths [5].
- *Rough surface*: surface is much rougher on the scale of the radar wavelength [5].

The observed signal, from the SAR system, is affected by interference due the phase differences between scatterers. Speckle can be seen as a interference phenomenon where the distribution of the phase terms is the main contributor of the noise-like structure [20]. Scatterers, from different positions of the resolution cell, could contribute with phase values quite different from each other. The phase term is conceivable as uniformly distributed as well as independent of A_i:

$$\phi \sim \mathcal{U}(-\pi, \pi) \tag{3.3}$$

Behind this assumptions the speckle signal is called *full developed speckle*. Moreover, by the *Central Limit Theorem*, the observed in-phase and quadrature components of the backscattered vector, $\Re(\mathbf{z}) = x = A\cos(\phi)$ and $\Im(\mathbf{z}) = y = A\sin(\phi)$, are *independent* and *identically Gaussian distributed* with zero mean and variance σ^2 [21].

$$x, y \sim \mathcal{N}(0, \sigma^2) \tag{3.4}$$

The joint *Probability Density Function* (PDF) is:

$$p_{x,y}(x, y) = \frac{1}{\pi\sigma^2} \exp\left(-\frac{x^2 + y^2}{\sigma^2}\right) \tag{3.5}$$

3.2.1 Radar Cross Section and Multi-look

Before analyzing the main task concurring speckle statistics, it is necessary to take into account two concepts the are used in the next section.

RCS defined in Section 2.3 as:

$$\sigma_{pq} = 4\pi \left| S_{pq} \right|^2 = 4\pi r^2 \left(\frac{P_S}{P_I} \right) \tag{3.6}$$

where pq represent the horizontal and vertical polarization respectively, r is the radar-target distance, P_I the incident power and P_S the scattered power. This parameter, as already said, is an area and is strongly dependent on frequency, polarization and incident angle. Moreover, RCS being an area, depends by the portion of the target illuminated from the radar system. In order to remove such a dependence it is defined the NRCS:

$$\sigma^0 = \frac{4\pi r^2}{A_0} \left(\frac{P_S}{P_I} \right) \tag{3.7}$$

where A_0 is the area of the illuminated surface where the phase can be considered constant enough. It is possible consider two case about σ^0:

- σ^0 is constant: *fine texture* or spatially uniform target.
- σ^0 is non uniform: *coarse texture* or spatially non-uniform target.

Texture describes the spatial variation of RCS and can be associated to groups of scatteres. It is taken in account in Section 4.2.3.

RCS is the information obtained from the SAR system, therefore we are interested to understand which one is the best estimator of it for a given pixel [21]. For a given in-phase and quadrature component, as in Equation 3.5, the *Maximum Likelihood Estimation* (MLE) of the RCS is:

$$\hat{\sigma} = x + y = I \tag{3.8}$$

Therefore, the MLE, at every pixel, is given from the observed intensity.

The Multilook Operation is used to reduce the speckle contribution.

RCS and the multilook operation are strongly connected to each other:

- A first case of multi-look is processing several measurements called *looks*, obtained from the same position, improving the σ estimation. Since σ is the mean power, this suggest that the correct approach, given L independent measurements, is to average the measurements in intensity [21] (for this reason in Section 3.2.2.2 will be considered the intensity distribution first). The operation maintains the mean intensity σ, but reduces the estimator variance to σ^2/L.
- The second case, still known as multi-look for having a better estimation of the parameter σ, is assuming a constant intensity behaviour in the L independent neighbourhoods of the pixel of interest.

In the first case the angular variation of the RCS is lost. Conversely, in the second case, the spatial variation worsens.

Finally, another merit of the multilook operation is about the resulting distribution which is well-know as the *Gamma Distribution*.

3.2.2 Single Channel Statistics

As defined in Section 2.3.1, the polarimetric data received from SAR is characterized by the *scattering matrix*:

$$\mathbf{S} = \begin{bmatrix} S_{HH} & S_{HV} \\ S_{VH} & S_{VV} \end{bmatrix} \tag{3.9}$$

The *single channel speckle statistic* about the *single-look case* is referred to the element S_{pq}, otherwise the *multi-look case* is referred about the corresponding average element expressed as C_{pq}.

3.2.2.1 Single-look Case

Amplitude is defined as: $A = \sqrt{x^2 + y^2}$.

Amplitude has a *Rayleigh Distribution* [22] proved in [23]:

$$p_A(A) = \frac{2A}{\sigma^2} \exp\left(-\frac{A^2}{\sigma^2}\right), \qquad A \geq 0 \tag{3.10}$$

The first and second moments are:

- $E[A] = \sigma\sqrt{\pi}/2$
- $Var(A) = (4 - \pi)\sigma^2/4$

There are two important point to mark:

- The ratio between standard deviation and mean value is completely independent of the parameter σ and it assumes an important position in the multiplicative speckle model which is treated in 3.2.4.

$$\frac{\sqrt{Var(A)}}{E[A]} = \frac{\sqrt{4-\pi}\sigma}{2}\frac{2}{\sigma\sqrt{\pi}} = \frac{\sqrt{4-\pi}}{\sqrt{\pi}} = 0.5227$$

- The *Rayleigh Probability Distribution* comes from the previous hypothesis about *no scatterers with reflected signal much stronger than the others*. Otherwise the signal follows the *Rice Probability Distribution* [24].

Intensity is defined as: $I = A^2 = x^2 + y^2$.

Intensity has a *Negative Exponential Distribution*:

$$p_I(I) = \frac{1}{\sigma^2} \exp\left(-\frac{I}{\sigma^2}\right), \qquad I \geq 0 \tag{3.11}$$

The first and second moments are:

- $E[I] = \sigma^2$
- $Var(I) = \sigma^4$

Intensity images are more likely to suffer a high contribution of speckle noise. It is established calculating the same ratio between standard deviation and mean value, shown in the amplitude case:

$$\frac{\sqrt{Var(A)}}{E[A]} = \frac{\sqrt{\sigma^4}}{\sigma^2} = 1$$

log-Intensity

$$D = ln(I) \tag{3.12}$$

log-Intensity has a *Fisher Tippet Distribution*:

$$p_D(D) = \frac{e^D}{\sigma} \, \text{exp}\Big(- e^D/\sigma \Big), \qquad I \geq 0 \tag{3.13}$$

The first and second moments are:

- $E[D] = \sigma - \gamma_E$
- $Var(D) = \pi^2/\sigma$

where γ_E is the *Euler's constant*.

3.2.2.2 Multi-look Case

Intensity The L-look average intensity is given by:

$$\bar{I} = \frac{1}{L}\sum_{i=1}^{L} I_i \tag{3.14}$$

where I_i are n independent variables exponentially distributed with mean value known.

Then the intensity multi-look has a *Gamma Distribution* :

$$p_{\bar{I}}\big(\bar{I}\big) = \frac{1}{\Gamma(L)}\left(\frac{L}{\sigma}\right)^L I^{L-1} \, \text{exp}\Big(- LI/\sigma \Big), \qquad I \geq 0 \tag{3.15}$$

The moments of order m is:

$$\big\langle I^m \big\rangle = \frac{\Gamma(m+L)}{\Gamma(L)}\left(\frac{\sigma}{L}\right)^m \tag{3.16}$$

The special case of the first and second order moments is:

- $E\big[\bar{I}\big] = \sigma$
- $Var\big(\bar{I}\big) = \sigma^2/L$

Amplitude The L-look average of the amplitude signal is useful for displaying the image. That is because, the dynamic range is reduced by doing the square root operatio. By applying the square root operation of the Gamma Distribution and the change of variable transformation, the amplitude PDF becomes:

$$P_{\bar{A}}\big(\bar{A}\big) = 2AP_{\bar{I}}\big(\bar{A}^2\big) = \frac{2}{\Gamma(L)}\left(\frac{L}{\sigma}\right)^L A^{2L-1} \, \text{exp}\Big(- LA^2/\sigma \Big), \qquad A \geq 0 \tag{3.17}$$

3.2.3 Single Channel Multiplicative Speckle Model

Taking into account about what was said in Section 3.2.1, all the information at each pixel is described by the mean power σ. Thus, the observed intensity at each pixel has the conditionally probability [21]:

$$P_I(I|\sigma) = \frac{1}{\sigma}\,\text{exp}\left(-\frac{I}{\sigma}\right), \qquad I \geq 0 \tag{3.18}$$

or

$$I = \sigma u \tag{3.19}$$

where u is exponentially distributed as:

$$P_u(u) = e^{-u}, \qquad n \geq 0 \tag{3.20}$$

Equation (3.19) is termed the *multiplicative model for speckle* and expresses the observed intensity I as a product of deterministic RCS.

3.2.4 Multi Channel Statistics

The *multi channel speckle statistics* of the *single-look case* refers to the vectorization of the matrix **S**, which is called $\boldsymbol{\Omega}$. Otherwise the *multi-look case* refers to the corresponding average matrix expressed as **C**.

3.2.4.1 Single-look Case

Hypothesising that the reciprocal medium and backscattering direction follow the BSA convention, the complex scattering vector (**S** matrix's vectorization) of *single elementary scatterers* may be represented by:

$$\boldsymbol{\Omega} = \begin{bmatrix} S_{HH} & \sqrt{2}S_{HV} & S_{VV} \end{bmatrix}^T \tag{3.21}$$

where the superscript T is the *transposition operator*, while H and V represent the horizontal and vertical wave polarization.

For a *distributed target* (extended area with an heavy number of scatters) the size of the considered resolution cell is larger compared to the radiation microwave's wavelength. Supposing the *Central Limit Theorem*, the scattering vector can be seen as a *Multivariate Complex Gaussian Distribution*:

$$p_{\boldsymbol{\Omega}}(\boldsymbol{\Omega}) = \frac{1}{\pi^3\,|\mathbf{C}|}\,\text{exp}(-\boldsymbol{\Omega}^H\mathbf{C}^{-1}\boldsymbol{\Omega}) \tag{3.22}$$

The complex covariance matrix is calculated as $\mathbf{C} = E\left[\boldsymbol{\Omega}\boldsymbol{\Omega}^H\right]$. It is an hermitian matrix, that means $\mathbf{C} = \mathbf{C}^H$. While $|\cdot|$ represents the *determinant operator* and the superscript H is the *hermitian operator*. Both the real and imaginary parts of any $\boldsymbol{\Omega}$ element have a *Circular Gaussian Distribution*. The follow condition, for the element $S_i = x_i + jy_i$, must be fulfilled:

- $E[x_i] = E[y_i] = 0$
- $E[x_i y_i] = 0$
- $E[x_i x_k] = E[y_i y_k]$
- $E[y_i x_k] = E[x_i y_k]$

Moreover the **C** matrix holds all the important information for describing the randomness of the scattering process, therefore it is able to fully describe the scattering vector $\boldsymbol{\Omega}$.

3.2.4.2 Multi-look Case

The expectation operator used for **C** estimation is not numerically achievable, but under the hypothesis of statistical ergodicity and stationarity, the MLE of the covariance matrix is obtainable using the multi-look computation (spatial averaging) of a collection of independent single-look covariance matrices **C**. Thus the relative multi-look covariance matrix is:

$$\mathbf{Z} = \left\langle \boldsymbol{\Omega}\boldsymbol{\Omega}^H \right\rangle_L = \frac{1}{L}\sum_{i=1}^{L} \boldsymbol{\Omega}_i \boldsymbol{\Omega}_i^H \tag{3.23}$$

where $\boldsymbol{\Omega}_i$ is scattering vector of the i-th sample, while L is the number of looks.

The estimated matrix has a *Complex Wishart Distribution*:

$$p_{\mathbf{Z}}^{(L)}(\mathbf{Z}) = \frac{L^{dL} \left|\mathbf{Z}\right|^{L-d} \exp\left[-L\,\mathrm{Tr}\left(\mathbf{C}^{-1}\mathbf{Z}\right)\right]}{K(L,d)\left|\mathbf{C}\right|^{L}} \tag{3.24}$$

where $\mathrm{Tr}(\cdot)$ represent the *trace operator* and the first denominator factor of Equation 3.24 is rewritable as:

$$K(L,d) = \pi^{\frac{1}{2}d(d-1)}\Gamma(L),\ldots,\Gamma(L-d+1) \tag{3.25}$$

Here, d is the vector $\boldsymbol{\Omega}$ dimension, that in the monostatic case analyzed is equal to $d = 3$, while $\Gamma(\cdot)$ is the *gamma function*.

3.2.5 Multi Channel Multiplicative Model

The multidimensional version of single channel speckle model, shown in Section 3.2.3, is given by the relation:

$$\boldsymbol{\Omega} = \mathbf{Cu} \tag{3.26}$$

where $\boldsymbol{\Omega}$ is the complex scattering vector, **C** is the part of covariance matrix that keeps all the necessary information and **u** represent the speckle vector, which has a different component in each channel.

PolSAR Data Simulation 4

PolSAR data and speckle noise are two inseparable concepts. Speckle noise is intrinsic in the PolSAR data acquisition, then it is not possible analyze an original version of data. For this reason a detailed comparison or evaluation among different filters is not allowed. A possible way to get around the problem, as written in [4], is simulating data using the Monte Carlo simulation method. The task of this procedure is to replicate, as much as possible, the heterogeneity and complexity of image structure and polarimetric information in real PolSAR data. The simulation involves two different work steps: *simulation and design of image structure* and *simulation of polarimetric information*.

4.1 Simulation and design of image structure

In [4], the image morphology is realised using a *Markov Random Field* (MRF) which considers only the stochastic character of the polarimetric information. instead we wish to realise a synthetic image structure keeping, as more as possible, the proprieties of a real image, giving attention to simulating real PolSAR issues as:

- Homogeneous areas: preservation of *radiometric information* and *edge between different areas*.
- Textured areas: preservation of *radiometric information* and *texture information (spatial signal variability)*.

The idea for achieving both these image structure tasks, polarimetric information and real image properties, is to divide the whole image in to several fairly large areas and then replace in each zone a specific polarimetric value, which is obtained from the same starter image.

The real polarimetric dataset used for this purpose, is the *Single Look Complex* (SLC) signal showed in Figure 4.1, over the area of the San Francisco Bay (CA). It is acquired by the *Airborne Synthetic Aperture Radar* (AIRSAR) instrument mounted aboard a modified NASA DC-8 aircraft [25]. During data collection, the plane flew at $8\ km$ over the average terrain height at a velocity of $215\ m/s$.

The SLC signal is too noisy to handle, so the first step is to make a multilook operation, with windows size 24×18, getting the relative *Multi Look Complex* (MLC) signal showed in Figure 4.1. The multilook operation's windows size should be enough large to remove the speckle contribution from the signal in such a way that assures the sampling of a non-noisy covariance matrix.

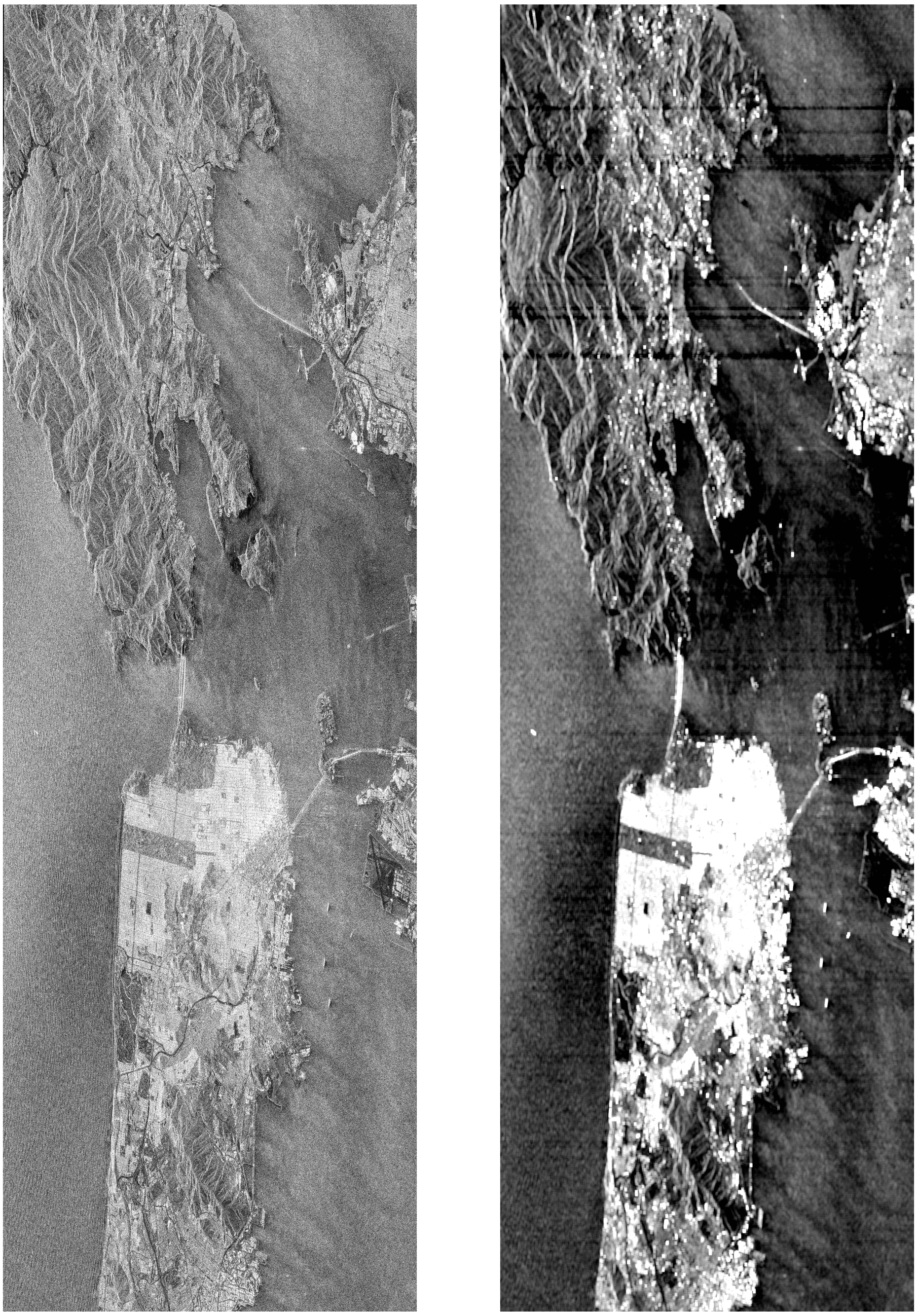

Figure 4.1: San Francisco Bay, SLC (left) and MLC (right).

First, the MLC has been segmented in five different heterogeneous areas: *urban*, *forest*, *field*, *ocean* and *river*. Second, each area has been classified with a label value as showed in Figure 4.2, which scope is just allow the identification of the areas.

4.2 Simulation of polarimetric information

4.2.1 Ground Truth

Real polarimetric information is obtained from the same image above, San Francisco Bay (CA). Using an optical image, the specific classes have been identified on the polarimetric image, then for every class a small portion of representative pixels has been sampled and stored, with a window size 20×20. Then the covariance matrix of each selected set of pixels has been averaged obtaining the five representative covariance matrices of the clusters. Hereinafter the representative covariance matrix will be called *cluster head* of the class. With the aid of the $H/A/\bar{\alpha}$ *Polarimetric Decomposition Theorem* [26] the computed cluster heads have been processed and further parameters *entropy*, *anisotropy* and the average angle $\bar{\alpha}$ have been extracted.

Covariance matrix values of cluster heads and the parameters $H/A/\bar{\alpha}$ are called *polarimetric signatures*. All the polarimetric signatures are introduced in Table 4.1.

Class	Covariance Matrix	$\boldsymbol{H/A/\bar{\alpha}}$
urban	$\begin{bmatrix} 2.9962 & 0.1828 - i0.0219 & 0.0409 - i0.0553 \\ 0.1828 + i0.0219 & 0.1598 & -0.0874 + i0.0035 \\ 0.0409 + i0.0553 & -0.0874 - i0.0035 & 1.9833 \end{bmatrix} \times 10^7$	$\begin{bmatrix} H = 0.7104 \\ A = 0.8651 \\ \bar{\alpha} = 45.8689° \end{bmatrix}$
forest	$\begin{bmatrix} 3.2316 & 0.0416 + i0.0469 & 1.0497 + i0.0151 \\ 0.0.416 - i0.469 & 7.8870 & -0.0083 - i0.0447 \\ 1.0497 - i0.0151 & -0.0083 + i0.0447 & 2.8157 \end{bmatrix} \times 10^6$	$\begin{bmatrix} H = 0.8714 \\ A = 0.3538 \\ \bar{\alpha} = 63.8666° \end{bmatrix}$
field	$\begin{bmatrix} 2.7588 & 0.0058 - i0.0527 & 1.4815 + i0.1026 \\ 0.0058 + i0.527 & 1.4663 & 0.0128 + i0.0222 \\ 1.4815 - i0.1026 & 0.0128 - i0.0222 & 2.8016 \end{bmatrix} \times 10^6$	$\begin{bmatrix} H = 0.8570 \\ A = 0.0640 \\ \bar{\alpha} = 36.1683° \end{bmatrix}$
ocean	$\begin{bmatrix} 2.7908 & -0.0315 - i0.0175 & 3.1147 - i0.0042 \\ -0.0315 + i0.0175 & 0.0671 & -0.0407 + i0.0193 \\ 3.1147 + i0.0042 & -0.0407 - i0.0193 & 3.8457 \end{bmatrix} \times 10^6$	$\begin{bmatrix} H = 0.1527 \\ A = 0.4109 \\ \bar{\alpha} = 7.5830° \end{bmatrix}$
street	$\begin{bmatrix} 2.7908 & -0.0315 - i0.0175 & 3.1147 - i0.0042 \\ -0.0315 + i0.0175 & 0.0671 & -0.0407 + i0.0193 \\ 3.1147 + i0.0042 & -0.0407 - i0.0193 & 3.8457 \end{bmatrix} \times 10^6$	$\begin{bmatrix} H = 0.1527 \\ A = 0.4109 \\ \bar{\alpha} = 7.5830° \end{bmatrix}$
target	$\begin{bmatrix} 990.02 & 4.97 & -7.04 \\ 4.97 & 0.02 & 0.04 \\ -7.04 & 0.04 & 0.05 \end{bmatrix} \times 10^7$	$\begin{bmatrix} H = NAN \\ A = NAN \\ \bar{\alpha} = NAN \end{bmatrix}$

Table 4.1: Polarimetric Signatures

Label masks can distinguish several zones, but still have polarimetric limitations. To solve the problem a mask capable to keep the polarimetric information is necessary. Take for example a generic pixel which has been questioned about its class membership. Then a new mask is created assigning, for the pixel with the same spatial position, the cluster head's value of that specific class. After repenting the process for each pixel, the new mask called *ground truth* showed in Figure 4.2 is able to distinguish several areas and in the same time it has polarimetric properties.

Therefore we obtained an image with real spaces as well as real shapes property and it can be seen as an agglomeration of homogenous polarimetric zones. Moreover the speckle contribution is absent, due to the way it is used for assigning the covariance matrix that distinguishes pixels.

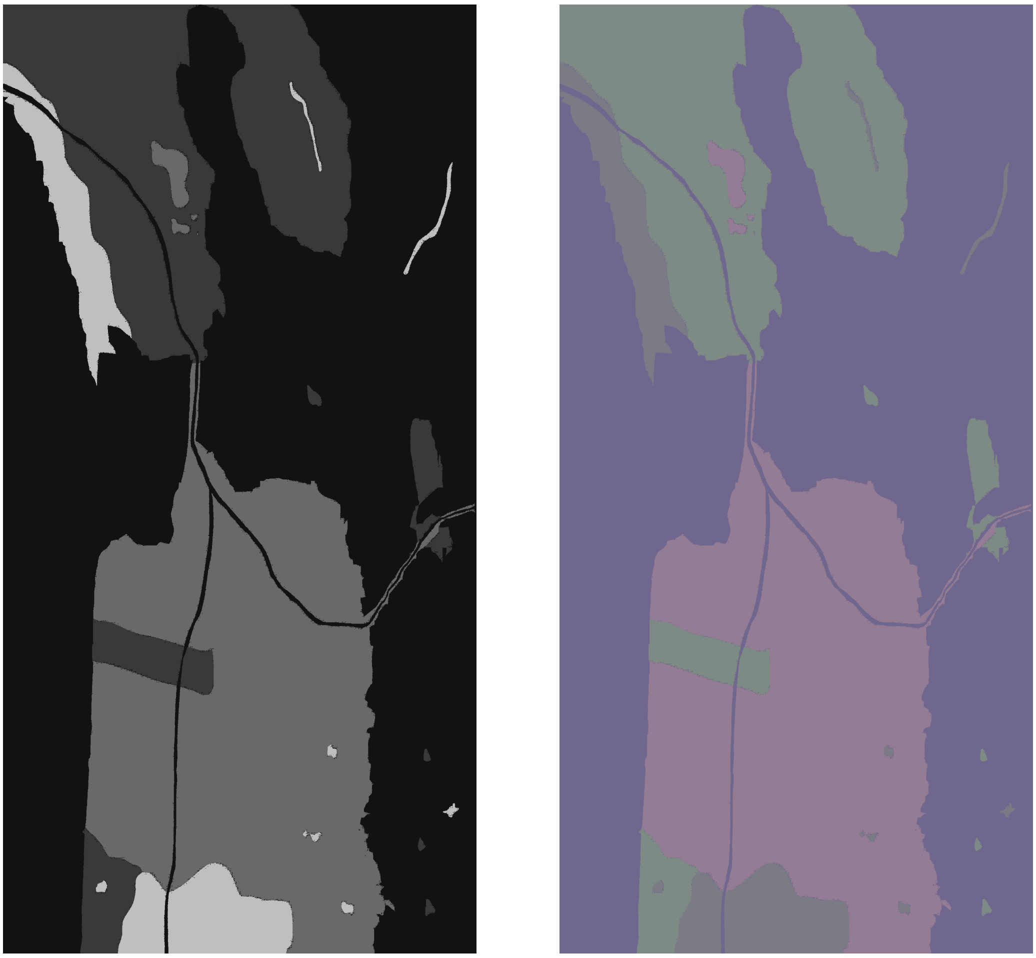

Figure 4.2: Label Mask (left), Pauli Decomposition Ground Truth (right).

4.2.2 Synthetic Data

The goal we set ourselves in the first part of Chapter 4 is being pursued, but as said above, PolSAR data and speckle noise are two inseparable concepts, hence it is necessary adding always speckle contribution to the ground truth. The most important concept behind it, is the different among a synthetic realization and to take an real image with natural speckle. In the first case it is possible to compare the noisy image with the same image noiseless. Whereas in the second case, it is impossible.

Monte Carlo Data Simulation In order to generate random PolSAR dataset, a *Choesky Decomposition* must be used as treated in [27] and [5], it allows to write a vector as a covariance matrix multiplied by random vector which represents the speckle contribute. The matrix **C** describes completely the scattering vector $\boldsymbol{\Omega}$, that is the concept on which the generation of a synthetic SLC will be based. First, as established in [28], it is necessary to generate a single-look vector $\boldsymbol{\Omega}$ from the covariance matrix $\mathbf{C} = E\left[\boldsymbol{\Omega}\boldsymbol{\Omega}^H\right]$ and finally average several simulations, obtainable with the Monte Carlo method, to get the multi-look data.

First, the covariance elements that hold the information are isolated:

$$\mathbf{C}^{1/2}(\mathbf{C}^{1/2})^H = \mathbf{C} \tag{4.1}$$

Second, generate a vector **u** which represents the speckle contribute. Thus, as defined in Equation 3.22, the random vector must be *Multivariate Complex Gaussian Distributed* with zero mean and identity covariance matrix **I**. That is realizable by generating, both real and imaginary components independently, as statistical independent normal distributed vectors with zero mean and variance $1/2$. The single-look vector is more easily created by multiplying the $\mathbf{C}^{1/2}$ and the vector **u**:

$$\boldsymbol{\Omega} = \mathbf{C}^{1/2}\mathbf{u} \tag{4.2}$$

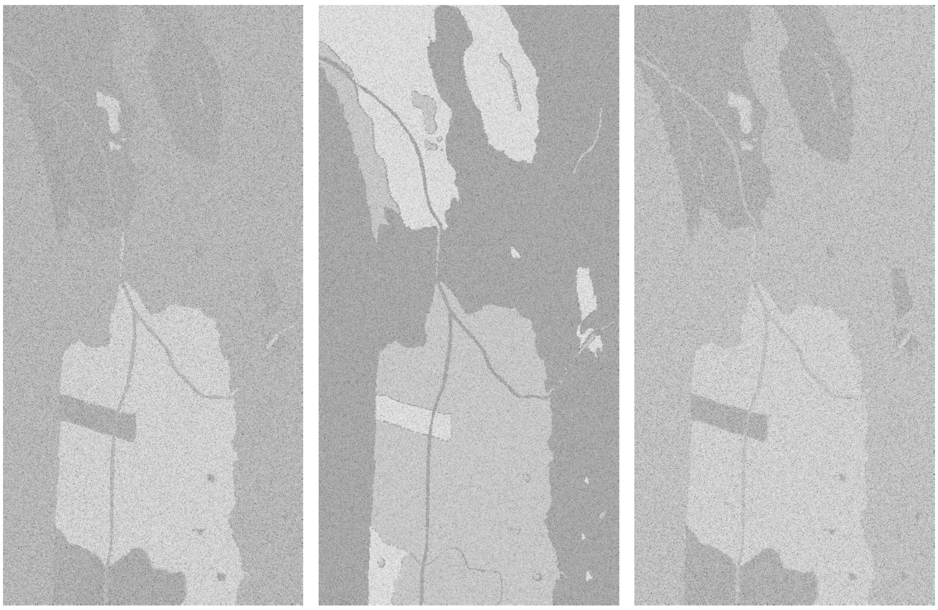

Figure 4.3: Synthetic single-look data: channel HH, channel HV and channel VV.

Finally, the multi-look data is obtained using the multilook operation:

$$\mathbf{Z} = \frac{1}{L}\sum_{i}^{L} \mathbf{\Omega}_i \mathbf{\Omega}_i^H \tag{4.3}$$

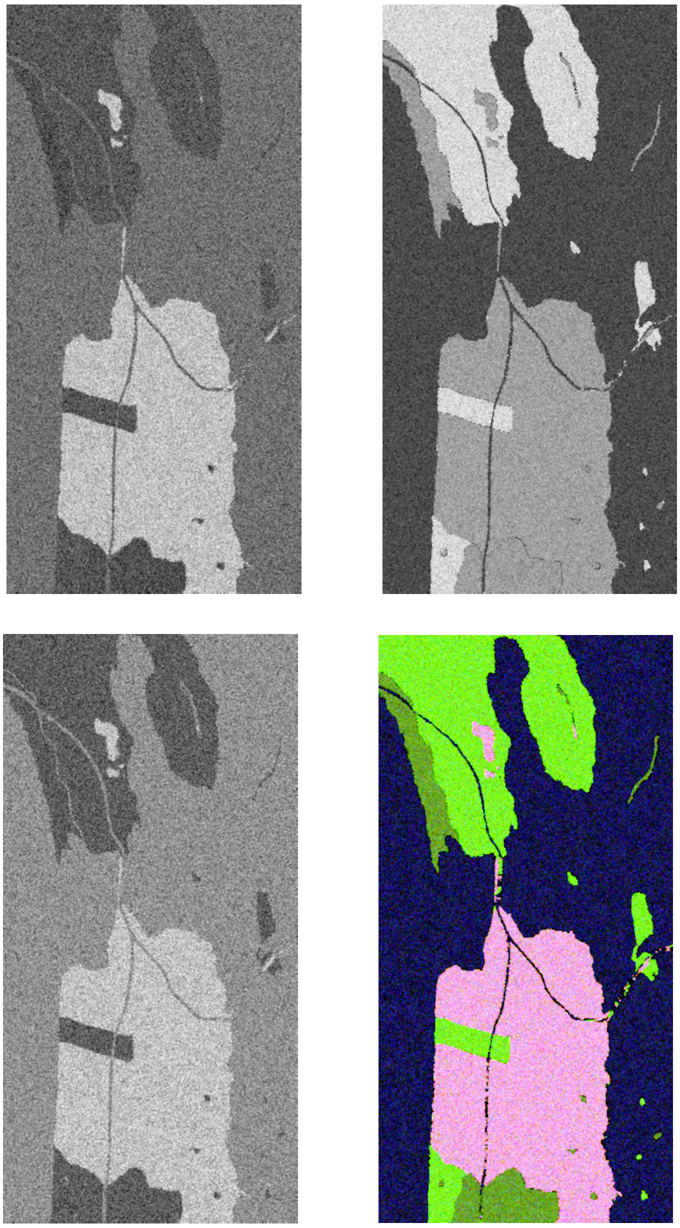

Figure 4.4: Synthetic multi-look data: channel HH (top-left), channel HV (top-right), channel VV (bottom-left) and Pauli Decomposition (bottom-right).

4.2.3 Texture

The simulation method made in Section 4.2.2 is allowed to realize data with polarimetric characteristics and a Rayleigh speckle model behaviour. All of it is a good approximation over homogenous areas, but in case of SAR systems with high resolutions over heterogeneous areas it is not capable to be realistic enough. For this reason, as opposed to [4], an extra signal has been added to simulate the surface variation. It is known as *texture*.

Texture Model The $\boldsymbol{\Omega}$ vector found in Section 4.2.2 for simulating speckle has a *Multivariate Complex Gaussian Distribution*:

$$\boldsymbol{\Omega} = \boldsymbol{\mu} + \mathbf{C}^{1/2}\mathbf{u}, \qquad \boldsymbol{\Omega} \sim \mathcal{N}^{\mathbb{C}}(\boldsymbol{\mu}, \mathbf{C}) \tag{4.4}$$

Then, for simulating the texture behaviour it is necessary to remake the Equation 4.4 with the texture variable τ [29]:

$$\boldsymbol{\Omega} = \boldsymbol{\mu} + \sqrt{\tau}\mathbf{C}^{1/2}\mathbf{u} \tag{4.5}$$

where $\boldsymbol{\mu}$ is the mean vector and $\mathbf{C}$ is the covariance matrix. The scale variable τ must be positive and real, it means $\sqrt{\tau}$ is a positive scalar factor. The conditional probability density function of $\boldsymbol{\Omega}$ given τ must still be a Multivariate Gaussian Complex Distribution as:

$$p_{\boldsymbol{\Omega}|\tau}(\boldsymbol{\Omega}|\tau) = \frac{1}{(2\pi\tau)^{d/2}} \exp\big[-\frac{1}{2\tau}(\boldsymbol{\Omega}-\boldsymbol{\mu})^H\mathbf{C}^{-1}(\boldsymbol{\Omega}-\boldsymbol{\mu})\big] \tag{4.6}$$

where d is the data dimension. Moreover, for simplicity $q(\tau)$ is defined as:

$$q(\boldsymbol{\Omega}) = (\boldsymbol{\Omega}-\boldsymbol{\mu})^T\mathbf{C}^{-1}(\boldsymbol{\Omega}-\boldsymbol{\mu}) \tag{4.7}$$

$\boldsymbol{\Omega}$ has different kind of distributions, which are directly linked to the texture distribution.

- **K-Distribution**

  It arises if the random variable τ is *Gamma distributed*.

  $$\tau \sim \Gamma(\alpha, \beta) \tag{4.8}$$

  The parameter α is known as *shape* and β as *rate*. The corresponding PDF in the shape-rate parametrization is:

  $$p_\tau(\tau, \alpha, \beta) = \frac{\beta^\alpha}{\Gamma(\alpha)}\tau^{\alpha-1}e^{-\beta\tau}, \qquad \tau > 0 \text{ and } \alpha, \beta > 0 \tag{4.9}$$

  where $\Gamma(\alpha)$ is a complete gamma function.

  Under the above assumption the SLC vector $\boldsymbol{\Omega}$ is *K-distributed* [30]:

  $$\boldsymbol{\Omega} \sim MK(\alpha, \beta, \boldsymbol{\mu}, \mathbf{C}) \tag{4.10}$$

  $$p_{\boldsymbol{\Omega}}(\boldsymbol{\Omega}, \alpha, \beta, \boldsymbol{\mu}, \mathbf{C}) = \frac{2}{(2\pi)^{d/2}}\frac{\beta^{\alpha+1}}{\Gamma(\alpha+1)}\left(\sqrt{\frac{q(\boldsymbol{\Omega})}{2\beta}}\right)^{\alpha+1-d/2} K_{\alpha+1-d/2}(\sqrt{2\beta q(\boldsymbol{\Omega})}) \tag{4.11}$$

  where $K_m(x)$ is a modified Bessel function of the second kind with order m.

- **$\mathcal{G}^0$-Distribution**

  It arises if the random variable τ is *Inverse Gamma distributed* [31] [32] [33].

$$\tau \sim \Gamma^{-1}(\lambda, \beta) \tag{4.12}$$

  The PDF is calculated as:

$$p_\tau(\tau, \lambda, \beta) = \frac{\beta^\lambda}{\Gamma(\lambda)} \tau^{-\lambda-1} e^{-\beta/\tau}, \qquad \tau > 0 \tag{4.13}$$

  where the parameters are the same of the previous distribution with the exception of λ than represent the new shape parameter.

  Under the above assumption the SLC vector $\mathbf{\Omega}$ is $\mathcal{G}^0$*-distributed* [34] [35]:

$$p_{\mathbf{\Omega}}(\mathbf{\Omega}, \lambda, \beta, \phi, \boldsymbol{\mu}, \mathbf{C}) = \frac{\phi^\phi \Gamma(\psi - \lambda)}{\beta^\lambda \Gamma(-\lambda)\Gamma(\phi)} \cdot \frac{\mathbf{\Omega}^{\phi-1}}{(\beta + \mathbf{\Omega}\phi)^{\phi-\lambda}} \tag{4.14}$$

  where $-\lambda, \beta > 0$ and $\phi \geq 1$.

- **U-Distribution**

  It arises if the random variable τ is *Fisher distributed* [36].

$$\tau \sim \mathcal{F}(\alpha, \lambda) \tag{4.15}$$

  For this distribution the PDF is:

$$p_\tau(\tau, \alpha, \lambda) = \left[\frac{(\alpha\tau)^\alpha \lambda^\lambda}{(\alpha\tau + \lambda)^{\alpha+\lambda}}\right] / \left[\tau B\left(\frac{\alpha}{2}, \frac{\lambda}{2}\right)\right], \qquad \tau \geq 0 \tag{4.16}$$

  where $B(\cdot)$ is the beta function.

  Under the above assumption the SLC vector $\mathbf{\Omega}$ is *U-distributed*.

As has already been said, according to the distribution of the random variable texture τ, the single-look vector Ω changes its distribution. This means that assuming a specific statistic behaviour of texture, all the simulated image change behaviour in turn. Usually in literature, the case studied since more time and than the case more known is texture Gamma distributed, which creates a single-look vector K-distributed. Because of that reason, the simulation has been implemented following the latter case. Obviously, future test can include texture simulation with different kind of distribution. In Figure 4.5 are shown the SLC channel HH, the MLC channel HH and the Pauli decomposition about the image with texture contribution.

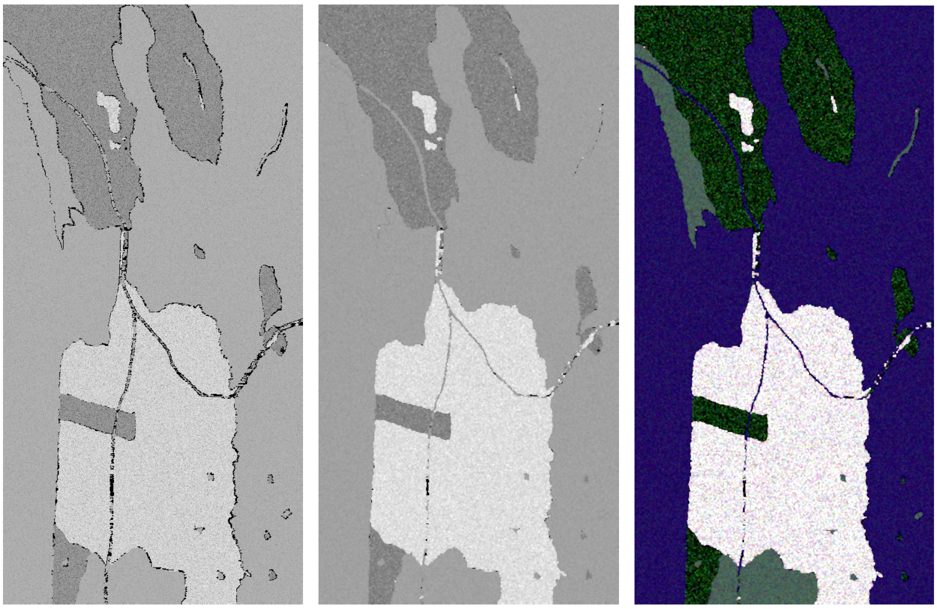

Figure 4.5: Synthetic textured data: SLC channel HH, MLC channel HH and Textured Pauli Decomposition.

4.2.4 Point Target

The last step to realize a realistic PolSAR image is to add *point targets* with different position and allocated in several data class. They have been added in both *ground truth* and *synthetic image*. Point targets correspond to square of size varying between 3×3, 5×5 and 7×7.

The **C** matrix that represent point targets is:

$$\mathbf{C}_{\text{point targets}} = \begin{bmatrix} 990.02 & 4.97 & -7.04 \\ 4.97 & 0.02 & 0.04 \\ -7.04 & 0.04 & 0.05 \end{bmatrix} \times 10^{7} \tag{4.17}$$

This matrix, for representing point targets, needs to have a special form:

- **C** has a deterministic scattering mechanism. That means a unique nonzero eigenvalue, to satisfy this property the rank of **C** should be equal to 1.
- The term C_{11} must have an high value. The HH channel has been chosen, but also HV and VV can be chosen.
- The term C_{12} is different from the zero value. That because this kind of scatters does not verify the symmetry reflection condition.
- The term C_{13} has real part less than zero [5]. This choice characterises the double-bounce scattering.

The points scatter have been added last in order to get over the speckle contribution. In Figure 4.6 are compared the Pauli decomposition of untexture image, the texture version and finally the texture version with point scatters. In Figure 4.7 are shown the final version of synthetic data with its ground truth.

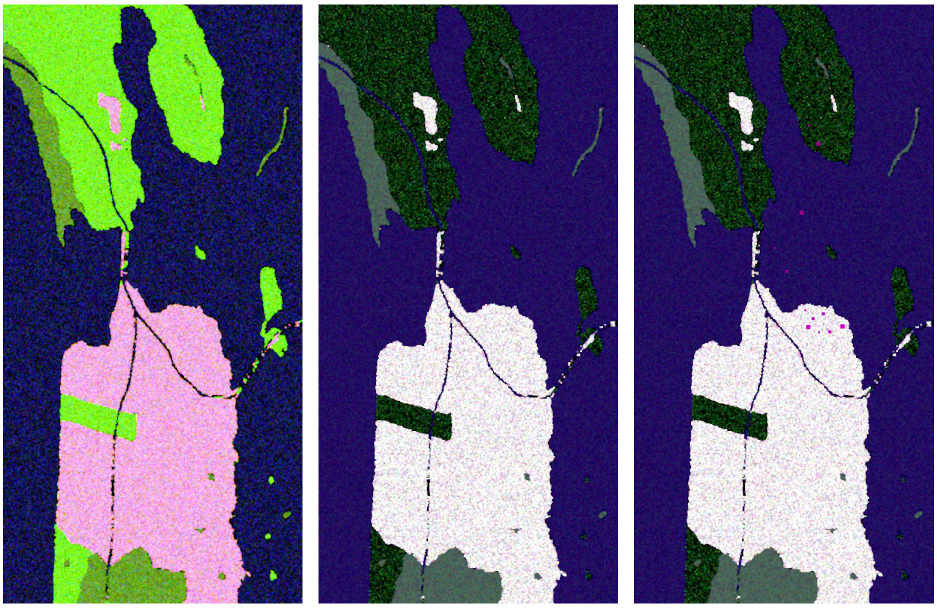

Figure 4.6: Synthetic textured data with target point: Untextured Pauli Decomposition, Textured Pauli Decomposition and Textured Pauli Decomposition with Target Point.

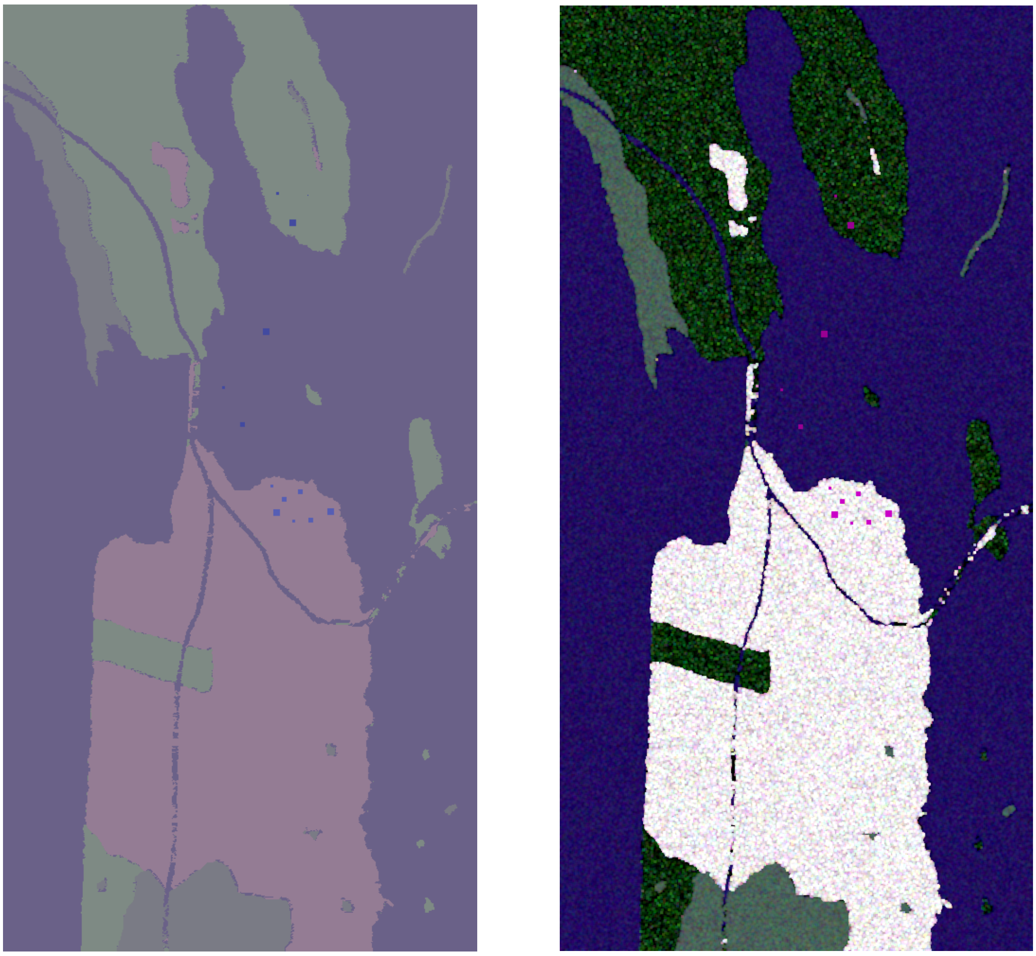

Figure 4.7: Final version of synthetic data: Ground Truth and Textured Pauli Decomposition with Target Point.

PolSAR Data Filters Analysis 5

The simulated images, generated as previously described in Chapter 4, are then filtered using all the filters described in Chapter 6. In order to have a meaningful evaluation of the filtering performances a numerical approach will be used. The filter output will be in the form of the covariance matrix **C**.

$$\mathbf{C} = \begin{bmatrix} C_{11} & C_{12} & C_{13} \\ C_{21} & C_{22} & C_{23} \\ C_{31} & C_{32} & C_{33} \end{bmatrix} \tag{5.1}$$

It is well-known that such a matrix is hermitian positive semidefinite. This fact has important implications:

- **C** satisfies the hermitian symmetry property: it equals its own conjugate transposed version $\mathbf{C} = \mathbf{C}^H$.
- **C** has real and non-negative eigenvalues.
- **C** has orthogonal eigenvectors.

In this way **C** is completely described by 3 real diagonal elements representing the polarimetric channel powers end 3 complex off-diagonal elements representing the correlations between polarimetric channels.

In other words, **C** is characterized by 9 parameters that will be named polarimetric parameters, as they describe *polarimetric information preservation*. It is important to remind that each pixel of a simulated image is characterized by its covariance matrix. It is remarkable to point out that the covariance **C** matrix, being Hermitian, contains all the polarimetric information in the elements along its diagonal and the elements in its upper triangular sub-matrix.

The filtering performances will be also evaluated in terms of *spatial information preservation*. In this case we will evaluate how and to what extent each pixel is correlated to its neighbour pixels. High correlation means low spatial variability among pixels. Such regions are usually named homogenous. Conversely low correlation means high spatial variability and are usually termed as heterogenous.

Following the approach proposed in [4], the evaluation parameters will be split in two subsets: *Polarimetric Information Evaluation* and *Spatial Information Evaluation*.

Moreover, the parameters are estimated considering their *absolute relative bias* for each different scattering class, due to the fact that effectiveness of PolSAR filtering depends on the scatterer itself. This way allows to override this issue.

5.1 Polarimetric Information Evaluation

- **Radiometric Parameters** (σ).

  They describe the RCS of the channels HH, HV and VV. Moreover they are related to the covariance matrix diagonal elements as follows:

  $$\sigma_{HH} = 4\pi C_{11} = 4\pi\left|S_{HH}\right|^2$$
  $$\sigma_{HV} = 4\pi C_{22} = 8\pi\left|S_{HV}\right|^2$$
  $$\sigma_{VV} = 4\pi C_{33} = 4\pi\left|S_{VV}\right|^2$$

- **Complex Correlation Parameters** (ρ).

  They describe the complex correlation across the channels using the complex off-diagonal elements $[C_{12}\ C_{13}\ C_{23}]$ [37]. Being complex parameters, they will be reported through the two terms of amplitude and phase.

- **Incoherent Decomposition Parameters** $(\boldsymbol{H/A/\hat{\alpha}})$.

  The three parameters *Entropy*, *Anisotropy* and the mean angle *Alpha* are the result of the polarimetric decomposition introduced in [16], which is able to give back information about the physical nature of the scattering mechanism irradiated from the target surface [17].

Procedure The test image simulated in Chapter 4 is characterized by 5 extended classes and one additional class composed by point targets, which is not considered in this context. In order to increase the statistical meaning of the performance evaluation, it is filtered 31 times, therefore the evaluation of a single bias shall consider each class l, each simulated image n of each filter $\mathcal{F}$ that is compared. The procedure exposed here is representing one the above parameters, then, without loss of generality, considers a generic parameter β and its estimated value $\hat{\beta}$. Radiometric parameters and complex correlation parameters are represented, in their turn, as three terms. For representing one of them, a generic term defined as β' is assumed. In case of incoherent decomposition parameters, obviously, β coincides with β'.

First, considering a specific filter and one of its simulated images, the absolute relative bias of the class l is calculated as:

$$\Delta_{\beta',l,n,\mathcal{F}} = \left|\frac{\beta'_l - \hat{\beta}'_l}{\beta'_l}\right| \tag{5.2}$$

We are hypothesising in addition to restrict the maximum bias value just found to 1. It prevents the special case where parameter β' has value identical or close to zero and then the determinator of Equation 5.2 makes a bias value slim to infinity.

Second, the bias of class l is evaluated with the same class bias of all the n images using the *median* operator. In other words it is a median of a specific class bias across all the simulated images.

$$\Delta_{\beta',l,\mathcal{F}} = \underset{n}{\text{median}}\{\min(\Delta_{\beta',l,n,\mathcal{F}}, 1)\} \tag{5.3}$$

Third, a further median operation is made across the scattered classes finding a single estimate value. That operation is made on each of classes and images, of the parameter β' of the filter $\mathcal{F}$:

$$\Delta_{\beta',\mathcal{F}} = \underset{C\in\Lambda_{es}}{\text{median}}\{\Delta_{\beta',n,\mathcal{F}}\} \tag{5.4}$$

where Λ_{es} is the set of all the points belonging an extended scatterer.

Finally, in order to find a unique parameter, a median operation is made across the three channels as:

$$\Delta_{\beta,\mathcal{F}} = \text{median}\{\Delta_{\beta',\mathcal{F}}, \Delta_{\beta'',\mathcal{F}}, \Delta_{\beta''',\mathcal{F}}\} \tag{5.5}$$

The number of simulated images and extended classes is taken deliberately as an odd number. In that case, the median operator orders the values into account and chooses the central value as set representative. This kind of evaluation has replaced the averaging operation for its reduced sensibility to outliers and moreover for decreasing the dependence among type of scattering process dependence and filtering performance.

- **Co-Polar and Cross-Polar Polarization Signatures (PS):**

  Evaluates the capability to measure the polarimetric signature, about any polarization basis, of a specific target. To find an expression about the polarimetric signature, it is necessary to start from the *Stokes Matrix* which permits the synthesis of a scattering cross section of a scatterer for any transmit and receive polarization signature [38]. As known, assuming a radio communication based on the reciprocity theorem hypothesis, the power absorbed by the load is:

$$P^{(r)} = K(\lambda,\theta,\phi)\begin{bmatrix}S_0\\S_1\\S_2\\S_3\end{bmatrix}^T [M] \begin{bmatrix}S_0\\S_1\\S_2\\S_3\end{bmatrix} \tag{5.6}$$

  where $K(\lambda,\theta,\phi)$ is a factor that accounts for the antenna gain and the effective area of it. Thus θ and ϕ denote the antenna's direction while λ is the wavelength. The Stokes parameters S expresse the polarization state in terms of *orientation angle* $\psi \in (-90, 90)$ and *ellipticity* angle $\chi \in (-45, 45)$:

$$\begin{aligned} S_1 &= S_0\cos(2\psi)\cos(2\chi)\\ S_2 &= S_0\sin(2\psi)\cos(2\chi)\\ S_3 &= S_0\sin(2\chi) \end{aligned} \tag{5.7}$$

  where S_0 is proportional to the total wave power and it represents the radius of the Poincarè sphere. Then, with this coordinate system, the transverse components of the electric field can be written using a complex 2×2 scattering matrix:

$$\begin{bmatrix}E_{H'}\\E_{V'}\end{bmatrix}^S = \frac{e^{jkr}}{r}\begin{bmatrix}S_{H'H} & S_{H'V}\\S_{V'H} & S_{V'V}\end{bmatrix}\begin{bmatrix}E_H\\E_V\end{bmatrix}^I \tag{5.8}$$

where H' and V' are the horizontal and vertical components of the scattered field, H and V refer to the incident field. The received power may also be expressed as an equivalent area, or scattering cross section of the scatterer:

$$\sigma_{ij} = \lim_{r \to \infty} (4\pi r^2) \frac{P_{ij}^{(r)}}{P^{(t)}} \tag{5.9}$$

Here the subscript ij represents the type of polarization: transmitted polarization j and received polarization i. Assuming moreover a normalized radiated electric field, $S_0 = 1$, the polarization ellipse of orientation angle and ellipticity angle, using the set of Equations 5.7 and 5.8, can be finally written as:

$$\sigma(\chi_i, \psi_i, \chi_j, \psi_j) = \begin{bmatrix} 1 \\ \cos(2\psi)\cos(2\chi) \\ \sin(2\psi)\cos(2\chi) \\ \sin(2\chi) \end{bmatrix}^T [M_{ij}] \begin{bmatrix} 1 \\ \cos(2\psi)\cos(2\chi) \\ \sin(2\psi)\cos(2\chi) \\ \sin(2\chi) \end{bmatrix} \tag{5.10}$$

Procedure The polarization signature estimator shall be considered far away from class boundaries, in other words it is necessary to extrapolate the stationariy areas from the simulated image and then to apply the estimator in those areas.

First, we calculate the co-polar and cross-polar signature, separately for each l class and for all the n images about a specific filter $\mathcal{F}$. In Figure 5.1 is shown an example of polarization signature from the *urban class* pixels.

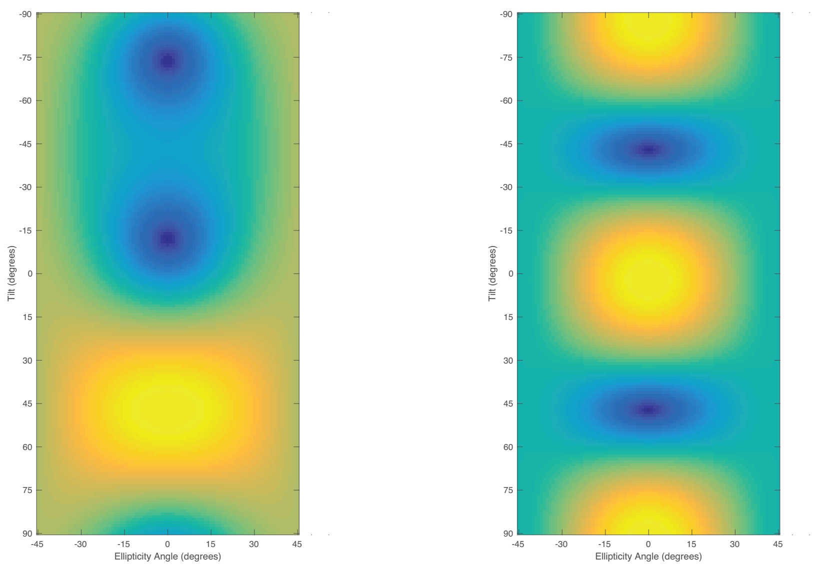

Figure 5.1: Polarization Signature: Co-Polar (left), Cross-Polar (right).

Second, for extracting the desired parameters for both of these matrices, as made in [39] and [40], the ellipticity angle has been set to 0, while the orientation angle is still varying. Then Equation 5.7 becomes:

$$\sigma(0,\psi) = \frac{1}{4}(\sigma_{hh}+\sigma_{vv})[1+\cos^2(2\psi)] + \frac{1}{2}(\sigma_{hh}-\sigma_{vv})\cos(2\psi) + \sigma_{hv} + \frac{1}{2}\Re[\sigma_{hhvv}]\sin^2(2\psi) \quad (5.11)$$

where σ_{HH}, σ_{HH} and σ_{HHVV} are the radar backscatter cross sections for horizontal, vertical and the correlation between horizontal and vertical polarization respectively. Therefore, the co-polar signature σ_{co} and the cross-polar signature σ_{cx} for each class l has been found.

Third, in order to generate a unique parameter, the co-polar and cross-polar signatures have been called β' and β'' respectively. Accordingly, the absolute relative bias of a given generic signature β' is:

$$\Delta_{\beta',l,n,\mathcal{F}} = \underset{\psi}{\text{median}}\left\{\frac{\beta'_l(\psi)-\hat{\beta}'_l(\psi)}{\beta'_l(\psi)}\right\} \quad (5.12)$$

Fourth, as made in Equation 5.3 and Equation 5.4, a median operation is computed through the simulated image and different scattering classes.

Finally, a global parameter is found by computing the mean value between the absolute relative bias of co-polar and cross-polar signatures:

$$\Delta_{\beta,\mathcal{F}} = \text{mean}\{\Delta_{\beta',\mathcal{F}}, \Delta_{\beta'',\mathcal{F}}\} \quad (5.13)$$

5.2 Spatial Information Evaluation

All the following parameters are calculated taking into account only power channels matching the diagonal elements of the covariance matrix, while the number of extended scatterers is identified as L.

- **Gradient Preservation (GP).**

  It is necessary to have a spatial derivation of each pixel. The resulting image, as shown in Figure 5.2, has zero values where the original image presented homogenous areas, therefore it has nonzero values in case of boundaries between extended targets [1].

  The gradient preservation parameter is able to evaluate the preservation of the boundaries in a generic channel i, as mentioned above, by averaging the ratio between the gradient values of the filtered channel intensity $\hat{I}_i$ and the respective gradient values of the ground truth I_i^* [4]:

$$GP(i) = \frac{1}{L}\sum_l \frac{\sum_{f(x)=l,|\nabla I_i^*(x)|>0} |\nabla \hat{I}_i(x)|}{\sum_{f(x)=l,|\nabla I_i^*(x)|>0} |\nabla I_i^*(x)|} \quad (5.14)$$

  where $f(x)$ is the class label for the pixel with position x and ∇ is the *Sobel Gradient Operator* [41] [42]. GP has values below 1 in case of an over-smoothed edge, instead, in case of speckle noise that is not sufficiently reduced or close over-smoothed point scatterers, GP can get largeer values.

[1] The showed values in Figure 5.2 are inverted for a stamp issue.

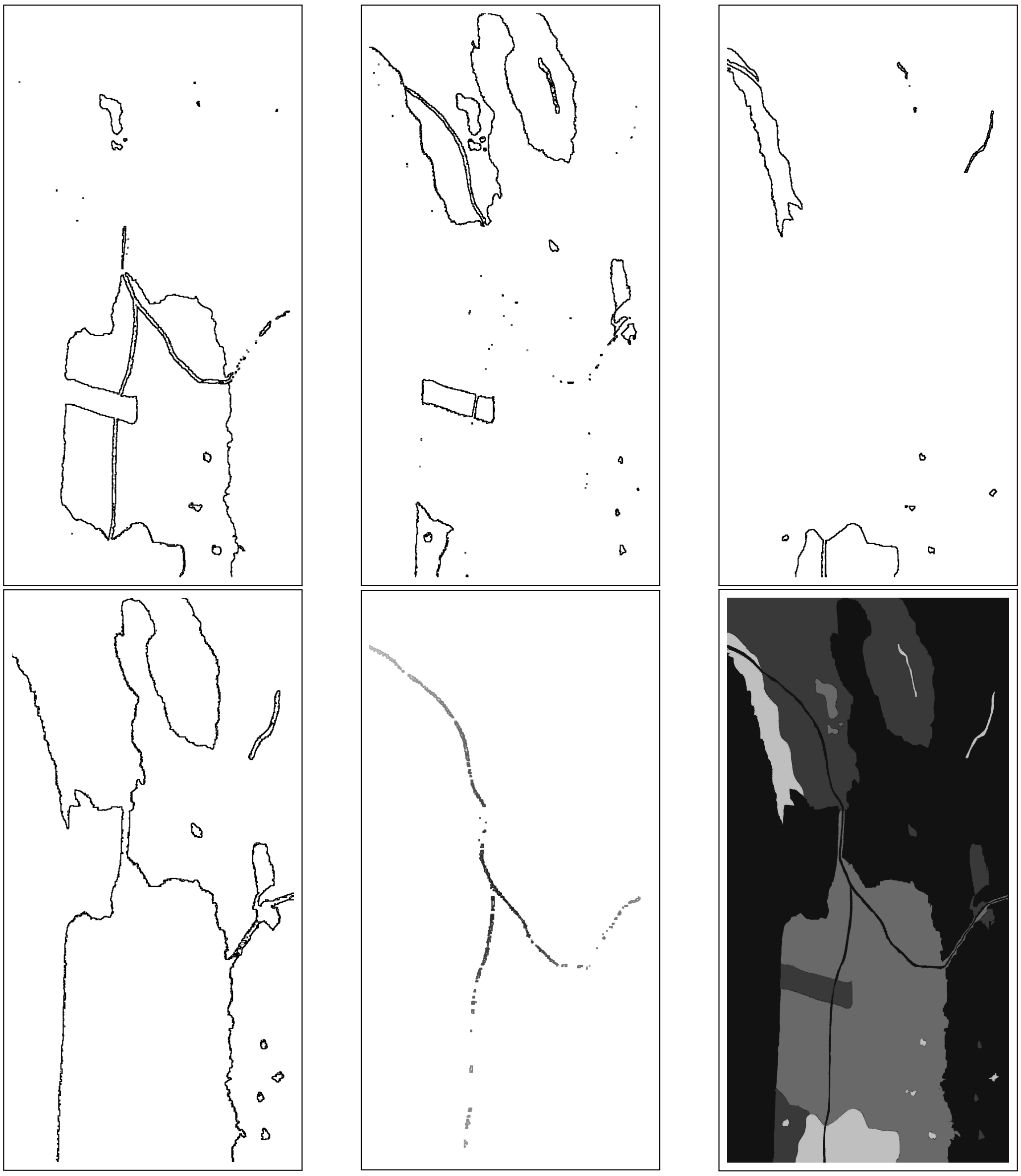

Figure 5.2: Class Edge: Urban (top-left), Forest (top-centre), Field (top-right), Ocean (bottom-left), River (bottom-centre) and Label Mask (bottom-right).

- **Edge Preservation** $(\boldsymbol{EP})$.

  Is a performance measure parameter [43] and it is highly bound with the gradient preservation because it is derived by mapping the values of that latter, over the interval $[0, 1]$, using triangular windows.

$$EP(i) = \begin{cases} 1 - \left|1 - GP(i)\right|, & GP(i) < 2 \\ 0, & GP(i) \geq 2 \end{cases} \tag{5.15}$$

  EP has small values in case of edge under-smoothing or over-smoothing.

- **Point Target Preservation (TP).**

  This parameters is specific for the evaluation about the visual preservation of point targets, for this reason it takes into account only the intensity of the pixels, where have been set the point targets, in both filtered image and ground truth.

$$TP = \sum_{j=1}^{m} \sum_{i=1}^{n} \frac{span(I_{ij})}{span(\hat{I}_{ij})} \tag{5.16}$$

  where m is the number of the target and n is the number of pixel about the i-th target. Moreover, I represents the ground truth and $\hat{I}$ the filtered image. Using the function $span(\cdot)$, the parameter TP takes into account the diagonal elements of the covariance matrix about each pixel of all point target.

- **Equivalent Number of Looks (ENL).**

  Quantifies, for all the power bands, the speckle noise reduction among extended scatterer [21]; in other words it shall not be considered the target point class. A general expression of the *Equivalent Number of Looks* (ENL) is:

$$ENL = \frac{E\{I_i\}^2}{Var\{I_i\}} = \frac{\langle I_i \rangle^2}{\langle I_i \rangle - \langle I_i \rangle^2} \tag{5.17}$$

  where I_i is the intensity about the channel i and $\langle \cdot \rangle$ denotes sample average [44].

  The three different channels and each classes need to be considered separately. The ENL channel value is calculated for each class l and finally the maximum value among the found ENLs is taken. Thus, for a generic sample image, the ENL form for the band i is:

$$ENL(i) = \max_{l} \left(\frac{\hat{\mu}_l^2}{\hat{\sigma}_l^2} \right) \tag{5.18}$$

Procedure In case of spatial preservation parameters, to generate a unique aggregated value for each filter $\mathcal{F}$, the following steps have been followed, while still using the generic parameter β.

First, as shown for each estimator description, a class evaluation is already made. All the parameters are expressed in terms of channel and then $\Delta_{\beta',n,\mathcal{F}}$ represents the parameter of a generic channel i and generic simulated image n of the filter $\mathcal{F}$.

Secondly the average across the power channel is computed:

$$\Delta_{\beta,n,\mathcal{F}} = \text{mean}\{\Delta_{\beta',n,\mathcal{F}}, \Delta_{\beta'',n,\mathcal{F}}, \Delta_{\beta''',n,\mathcal{F}}\} \tag{5.19}$$

Finally, a median operation is applied across all the simulated images:

$$\Delta_{\beta,\mathcal{F}} = \underset{n}{\text{median}}\{\Delta_{\beta,n,\mathcal{F}}\} \tag{5.20}$$

Result 6

In this Chapter has been taken the synthetic image made in Chapter 4 which has been processed through several filters ($\mathcal{F}$) listed below. The result of each filter has been evaluated using the parameters (Δ_β) made in Chapter 5. The evaluation of each filter has been repeated changing intrinsic properties of the filter itself. The best combination of properties for each filter are shown in Table 6.1, moreover are highlighted the best values for each parameter considering all the filters. After the whole estimation presentation, each filter is evaluated by itself plotting the values of the parameters in a *radar chart* which is useful for having a visual global consideration.

An important note to point out is that each parameter is obtained as a bias:

$$\Delta_\beta = \left| \frac{\beta - \hat{\beta}}{\beta} \right| \tag{6.1}$$

where β is the parameter taken from the *ground truth* and $\hat{\beta}$ is the parameter taken from the *filtered image*. Low value of Δ_β means that the filter in question does not distort too much the signal. Conversely, high value of Δ_β means a filtering which introduces distortion.

$\mathcal{F}$ | Δ_β	σ	$\|\rho\|$	$\angle\rho$	H	A	$\bar{\alpha}$	PS	GP	TP	ENL
Boxcar 5	6.80	18.76	6.02	7.76	11.88	7.81	10.62	3.06	6.20	12.37
Boxcar 7	5.85	14.73	6.83	6.53	7.96	7.58	8.37	4.49	9.13	16.06
Gaussian 5	6.14	18.48	4.22	9.67	21.30	8.24	9.22	7.89	6.92	13.89
Gaussian 7	4.06	**13.49**	6.04	7.50	11.36	7.37	7.38	4.70	5.75	17.70
Lee Sigma 5	2.55	16.33	2.71	100	100	15.76	9.48	19.66	7.25	18.21
Lee Sigma 7	3.36	14.86	2.84	100	100	14.73	7.19	19.56	**4.97**	13.76
Lee Refined 7	8.38	17.02	**2.42**	16.31	20.71	11.60	9.33	10.75	7.47	11.57
Lee Refined 9	6.74	16.43	3.18	15.62	19.15	10.34	7.08	10.80	6.01	9.60
Lopez 7	9.85	32.76	4.94	**5.46**	5.76	5.47	7.73	3.06	7.51	3.56
Lopez 9	13.13	19.38	6.58	5.84	**4.22**	**4.82**	**6.98**	**2.34**	7.46	**2.24**
NLM Sigma 5	**0.97**	21.08	3.00	64.04	100	17.95	13.26	18.39	6.83	17.39
NLM Sigma 7	1.55	20.15	3.67	59.98	100	17.74	14.18	18.30	6.44	16.30
NLM Refined 7	1.41	30.12	5.60	58.94	100	13.04	14.05	15.99	6.83	17.58
NLM Refined 9	1.58	21.11	6.08	56.21	100	12.57	14.65	15.85	6.83	16.32

Table 6.1: Result of Filtering Operation.

6.1 Boxcar Filter

The *boxcar filter*, also known as *multilook*, is based on the MLE of the covariance matrix **C**. The algorithm can be seen as a window, which scrolling over all the image, replaces the center pixel value with the average of the selected samples by the window. Conceptually it is a low-pass filter which improves the *radiometric resolution*, due to the speckle decreasing, at the expense of *spatial resolution*, due to the downsampling. Spatial resolution decrease is, in a general way, inversely proportional to the size of the window.

The best values of the polarimetric parameters is given by a 7×7 window size. Theoretically the 3×3 window size should be better in therms of spatial resolution, but the contribute of speckle is still to high. Otherwise 7×7 and 9×9 window size decreases enough the speckle contribute, but its dimension does not allows a better spatial preservation then the 5×5 windows.

$\mathcal{F} \mid \Delta_\beta$	σ	$\|\rho\|$	$\angle\rho$	H	A	$\bar{\alpha}$	PS	GP	TP	ENL
Boxcar 5	6.80	18.76	6.02	7.76	11.88	7.81	10.62	3.06	6.20	12.37
Boxcar 7	5.85	14.73	6.83	6.53	7.96	7.58	8.37	4.49	9.13	16.06

Table 6.2: Result of Boxcar Filter.

The generality of this filter is evident by the radar chart as well. Both of the filters have values which generate an interpolation lines never too close or too far from the center of the chart.

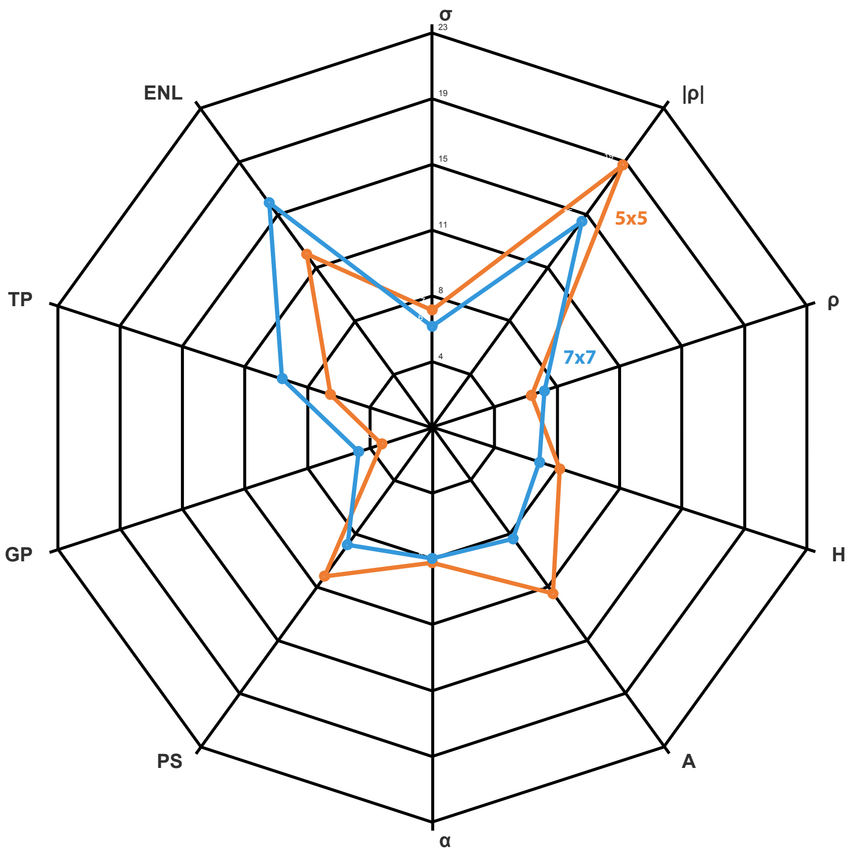

Figure 6.1: Radar Chart of Boxcar Filter.

The original image and the filtered images are shown in Figure 6.2.

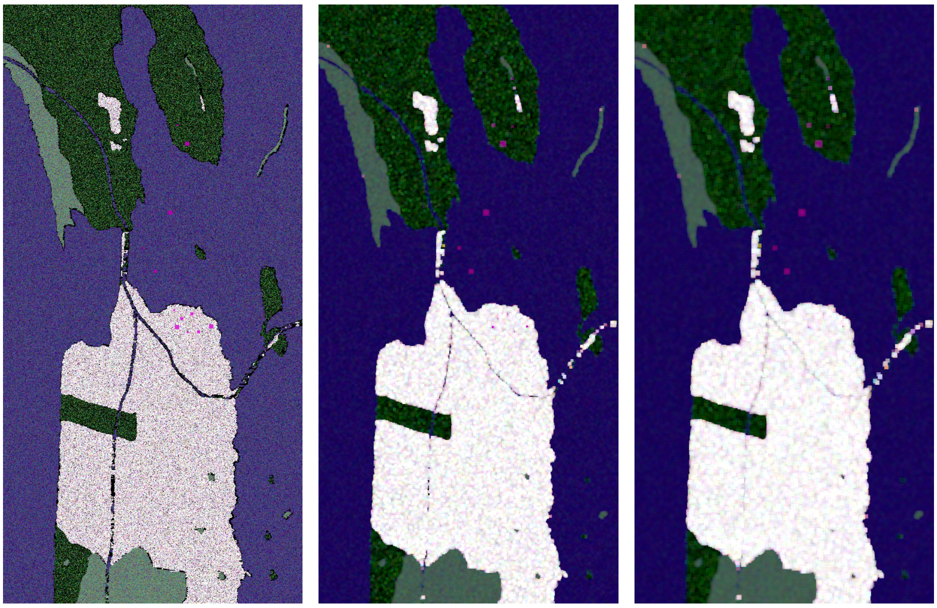

Figure 6.2: Filtering Boxcar: unfiltered, filtered [5x5], filtered [7x7].

6.2 Gaussian Filter

Gaussian filter can be seen as a refining of the *boxcar filter*, they are both base on the same concept: *Maximum Likelihood Estimation* (MLE) on the covariance matrix **C**. There is a little niggles in the way to weigh the samples involved in the average operation. In the boxcar case, considering a 3×3 square window, the average of the 9 samples will be the future value of the center pixel. Conversely, in the gaussian case, the window before mentioned has a 2D gaussian distribution. Thus, in the average operation, the value of the center pixel has more weight then the other pixels.

Gaussian filter, using a 7×7 window size, obtains the best estimation of the amplitude of complex correlation parameter $|\rho|$ and good value of point target preservation TP. The 5×5 window, compared with the 7×7 window, has better value just in two case: phase of complex correlation parameter $\angle\rho$ and the equivalent number of looks ENL. Moreover, 5×5 window has one of the worst value of the anisotropy A. The *Non Local Mean Filter* (NLMF) have a saturation of the anisotropy parameter. It is of course worst than the gaussian filter, but in the future the problem could be analyzed and maybe solved.

$\mathcal{F} \mid \boldsymbol{\Delta}_{\beta}$	σ	$\lvert\rho\rvert$	$\angle\rho$	H	A	$\bar{\alpha}$	PS	GP	TP	ENL
Gaussian 5	6.14	18.48	4.22	9.67	21.30	8.24	9.22	7.89	6.92	13.89
Gaussian 7	4.06	**13.49**	6.04	7.50	11.36	7.37	7.38	4.70	5.75	17.70

Table 6.3: Gaussian Filter Result.

The parameters distribution on the radar chart is similar to the boxcar filter. The interpolation lines never too close or too far from the center of the chart, but contrary there are some exception due to peaks. The positive peaks are $|\rho|$ and TP, instead the negative peak is A.

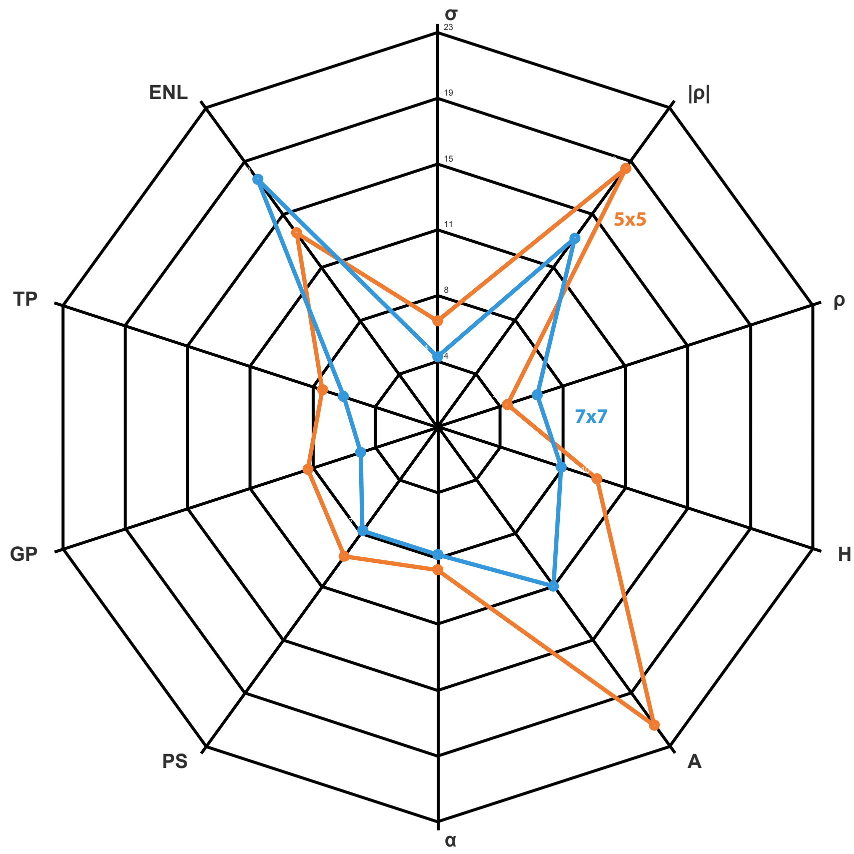

Figure 6.3: Radar Chart of Gaussian Filter.

The original image and the filtered images are shown in Figure 6.4.

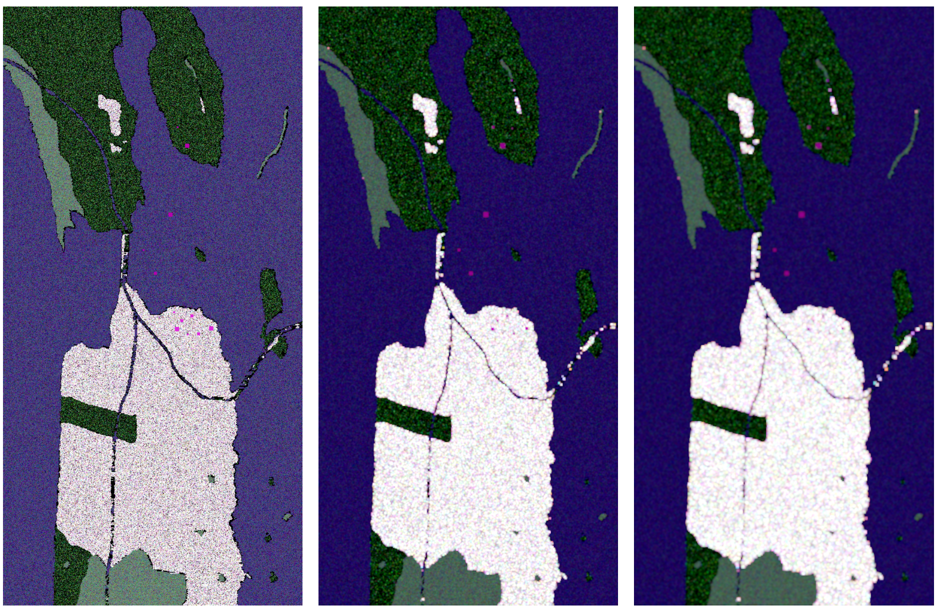

Figure 6.4: Filtering Gaussian: unfiltered, filtered [5x5], filtered [7x7].

6.3 Lee Sigma Filter

The *Lee sigma filter*, more simply called *Lee filter*, uses the data model to apply the despeckling operation. The multiplicative noise model has been linearized about the mean of the noisy signal for obtaining the *Linear Minimum Mean Square Error* (LMMSE) solution [19]. The Lee algorithm approximates the exact solution less than the quantity:

$$(1 + \sigma_u^2)^{-1} \tag{6.2}$$

where, referring to Equation (3.19), the term σ_u^2 is the variance of the multiplicative noise u. Being $\sigma_u^2 \ll 1$, in case of *multi-look* images, the contribution is meaningless [45].

Lee filter obtains the best value of point target preservation TP. Moreover it as good values of radiometric parameters σ and complex correlation parameters $|\rho|$. Conversely, the incoherent decomposition parameters H/A have a saturation to the upper limit.

$\mathcal{F} \mid \Delta_\beta$	σ	$\|\rho\|$	$\angle\rho$	H	A	$\bar{\alpha}$	PS	GP	TP	ENL
Lee Sigma 5	2.55	16.33	2.71	100	100	15.76	9.48	19.66	7.25	18.21
Lee Sigma 7	3.36	14.86	2.84	100	100	14.73	7.19	19.56	**4.97**	13.76

Table 6.4: Lee Sigma Filter Result.

The radar chart shows clearly that the 7×7 window returns a better filtering compared with the 5×5 window.

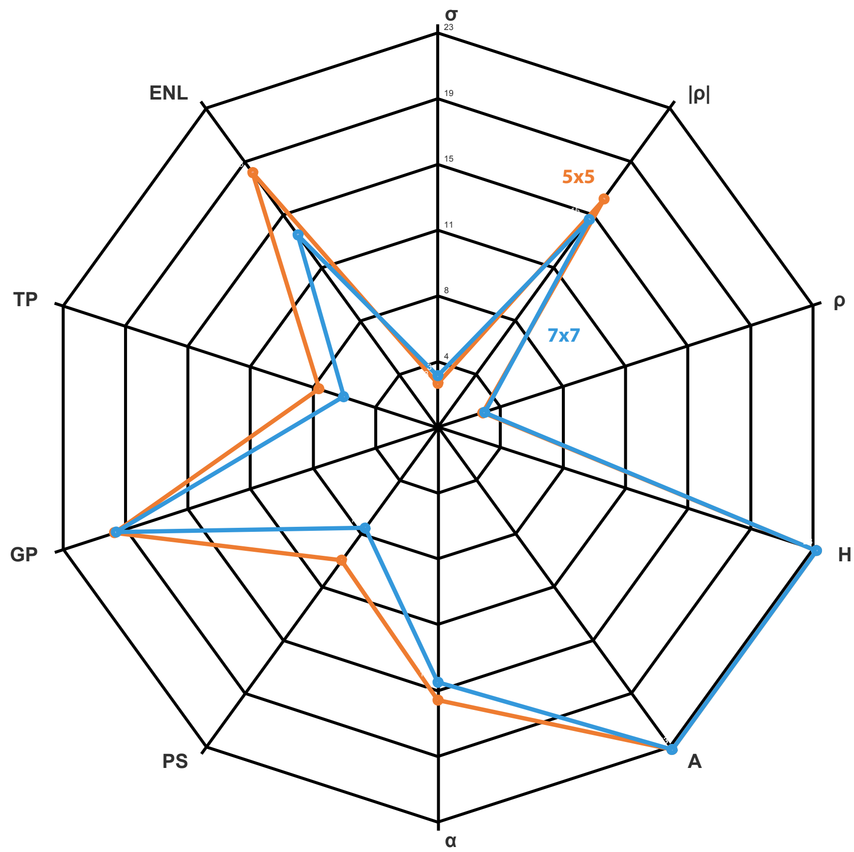

Figure 6.5: Radar Chart of Lee Sigma Filter.

The original image and the filtered images are shown in Figure 6.6.

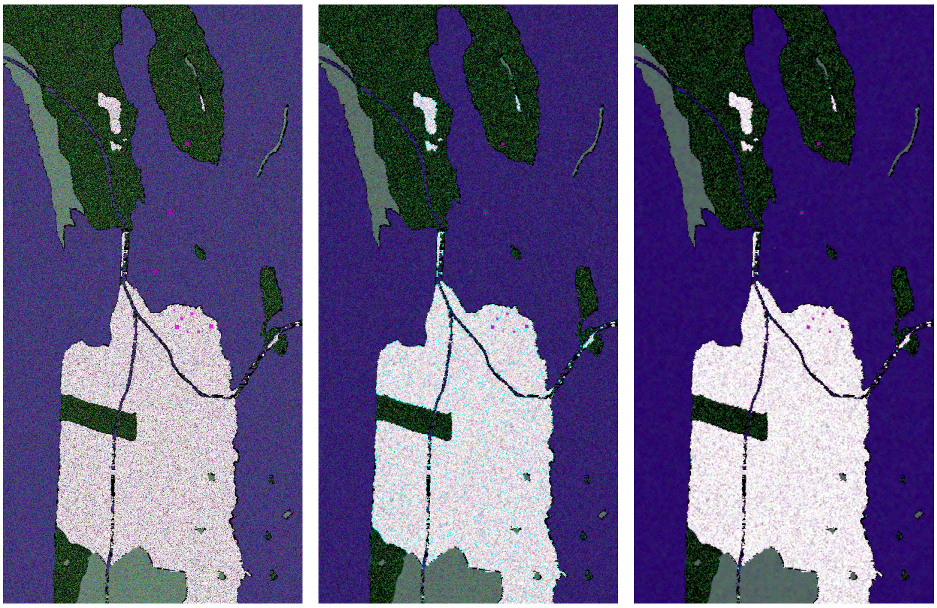

Figure 6.6: Filtering Lee Sigma: unfiltered, filtered [5x5 - 3 look], filtered [7x7 - 5 look].

6.4 Lee Refined Filter

The *Lee Refined Filter* has been created to fix the drawback of edge boundaries, which are not removed by Lee filter. Moreover the Lee refined filter use a window with minimum size equal to 7×7. The following process may be easy extended to larger windows. The center pixel is filtered choosing one of the edge-aligned windows shown in Figure 6.7.

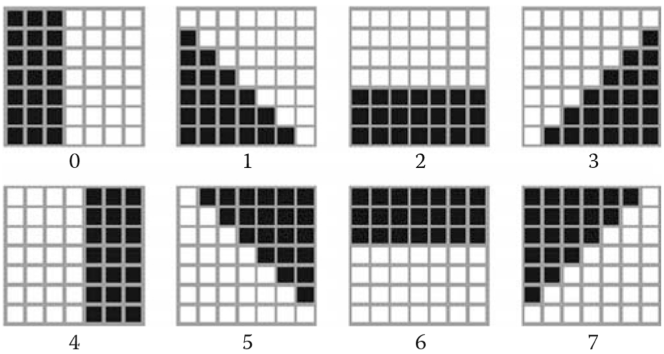

Figure 6.7: Edge-aligned windows.

In the windows, only the pixels relevant to the white pixels, are considered in the filtering operation. The shape of pixels chosen for filtering have similar radiometric property compared to the center pixel. That means a better noise filtering and a decreased blurred effect. The 7×7 window is split, Figure 6.8, in nine sub-windows, which have a dimension of 3×3. An local gradient algorithm, applied to the 3×3 windows, detects the edge orientation of the pixels selected by the whole 7×7 windows and finally the mean is calculated using a *Local Linear Minimum Mean Square Error* (LLMMSE) [46].

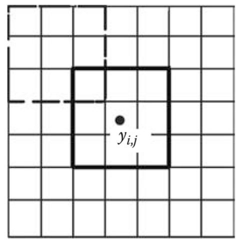

Figure 6.8: Edge-aligned sub-windows.

Numerically, the Lee refined filter has lower values then the simple Lee filter. Moreover, the 7×7 refined filter, obtain the minimum value of the phase of the complex correlation parameter $\angle\rho$.

$\mathcal{F} \mid \Delta_\beta$	σ	$\|\rho\|$	$\angle\rho$	H	A	$\bar{\alpha}$	PS	GP	TP	ENL
Lee Refined 7	8.38	17.02	**2.42**	16.31	20.71	11.60	9.33	10.75	7.47	11.57
Lee Refined 9	6.74	16.43	3.18	15.62	19.15	10.34	7.08	10.80	6.01	9.60

Table 6.5: Lee Refined Filter Result.

As opposed to Lee filter, the radar chart shows that the parameters H/A have a normal value without the limit case of saturation.

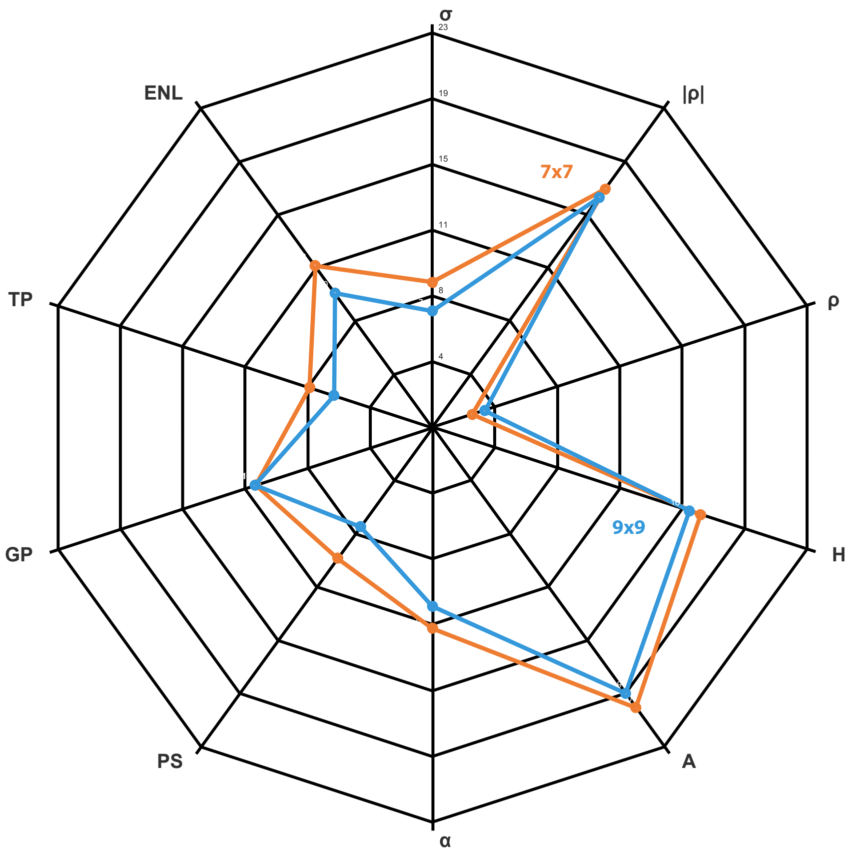

Figure 6.9: Radar Chart of Lee Refined Filter.

The original image and the filtered images are shown in Figure 6.10.

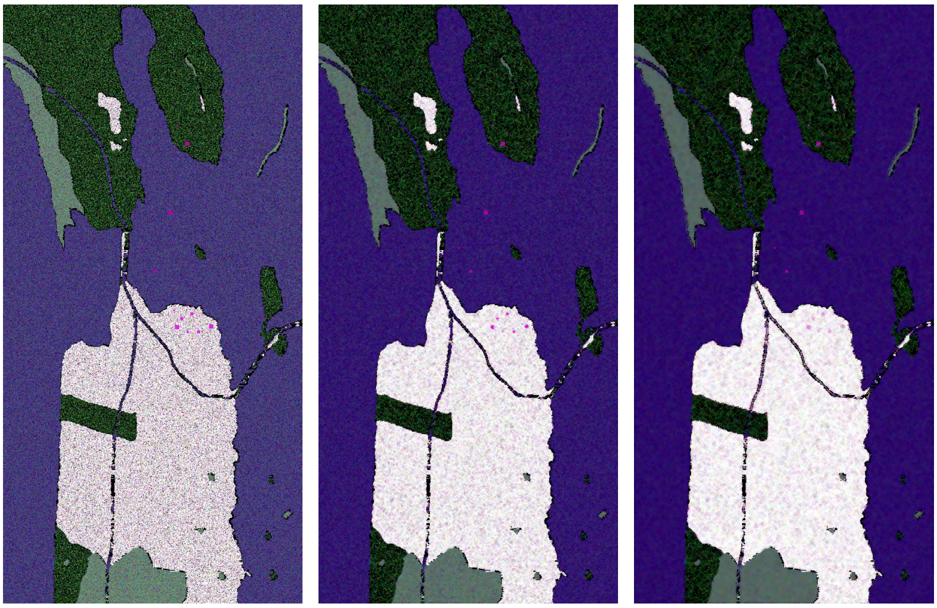

Figure 6.10: Filtering Lee Refined: unfiltered, filtered [7x7 - 5 look], filtered [9x9 - 5 look].

6.5 Lopez Filter

The *Lopez filter* has been the best filter of the whole filtering operation. It obtained the best estimation of six parameters out of a total of ten parameters.

Taking into account the case of a 7×7 window size, Lopez filter produce the best value of the entropy parameter H. Instead, the case of a 9×9 window size, produce the best values in term of anisotropy A, the mean of the angle alpha $\hat{\alpha}$, the polarization signature preservation PS, the gradient preservation GP and finally the equivalent number of looks ENL.

An important observation to point out is that, the values of radiometric parameters σ and both complex correlation parameters $|\rho|$ and $\angle\rho$, are far to assume good values.

$\mathcal{F}$ | Δ_β	σ	$\|\rho\|$	$\angle\rho$	H	A	$\bar{\alpha}$	PS	GP	TP	ENL
Lopez 7	9.85	32.76	4.94	**5.46**	5.76	5.47	7.73	3.06	7.51	3.56
Lopez 9	13.13	19.38	6.58	5.84	**4.22**	**4.82**	**6.98**	**2.34**	7.46	**2.24**

Table 6.6: Lopez Filter Result.

The radar chart, conversely with the filters analyzed until now, has a shape deep focused to the center of the chart. The unique exception is given by two lobes in direction of σ and $|\rho|$. To be more specific, the filtering made by the 7×7 window size reach the worst value of $|\rho|$.

Other one observation is about the point target preservation. A quickly look of the filtered image in Figure 6.12, shows a good point target preservation in both of the case. There is an obvious decreasing of preservation in proximity of *urban areas*.

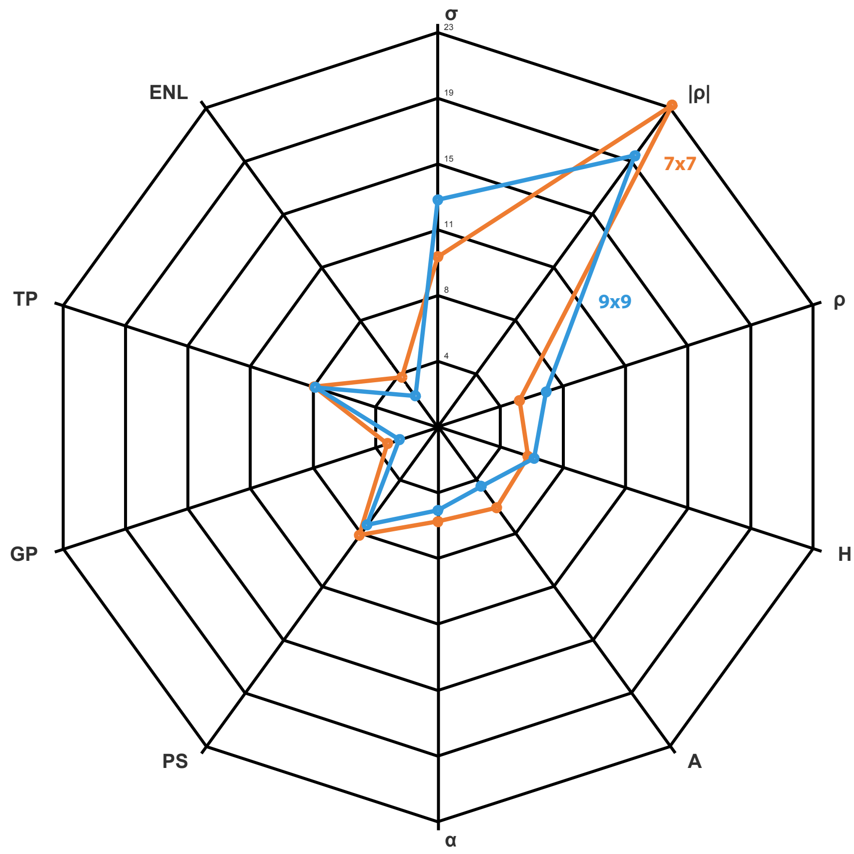

Figure 6.11: Radar Chart of Lopez Filter.

The original image and the filtered images are shown in Figure 6.12.

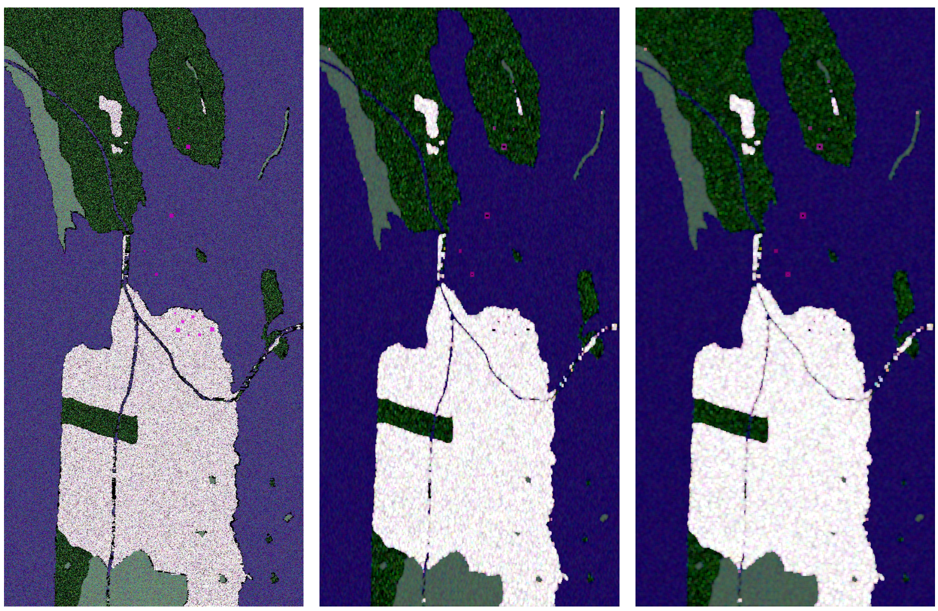

Figure 6.12: Filtering Lopez: unfiltered, filtered [7x7 - 5 look], filtered [9x9 - 3 look].

6.6 Non Local Mean Sigma Filter

The concept of *Non Local Mean Filter* (NLMF) is to estimate the original image by a weighted average of the noisy image. Referring to Equation (3.19), the estimation is given by:

$$\hat{\sigma} = \frac{\sum_m w(n,m)I(m)}{\sum_m w(n,m)}, \qquad w(n,m) = \exp\left(-\frac{1}{h}\sum_k a_k \left|I(n+k) - I(m+k)\right|^2\right) \tag{6.3}$$

where w represent the weight function, which take into account the Euclidean distance about two samples of the noisy image: $I(n)$ and $I(m)$. Moreover, h controls the decay of the exponential function and a_k defines a Gaussian window [19] [47]. This procedure has been applied to the *Lee Sigma filter* first and next to the *Lee Refined filter*.

The *Non Local Mean Lee Sigma Filter* obtained the best value of the radiometric parameters σ. There are remarkable values of $\angle\rho$ and TP.

$\mathcal{F}$ | Δ_β	σ	$\|\rho\|$	$\angle\rho$	H	A	$\bar{\alpha}$	PS	GP	TP	ENL
NLM Sigma 5	**0.97**	21.08	3.00	64.04	100	17.95	13.26	18.39	6.83	17.39
NLM Sigma 7	1.55	20.15	3.67	59.98	100	17.74	14.18	18.30	6.44	16.30

Table 6.7: Non Local Mean Sigma Filter Result.

The radar chart highlights the weakness in term of H and A, which have been saturated.

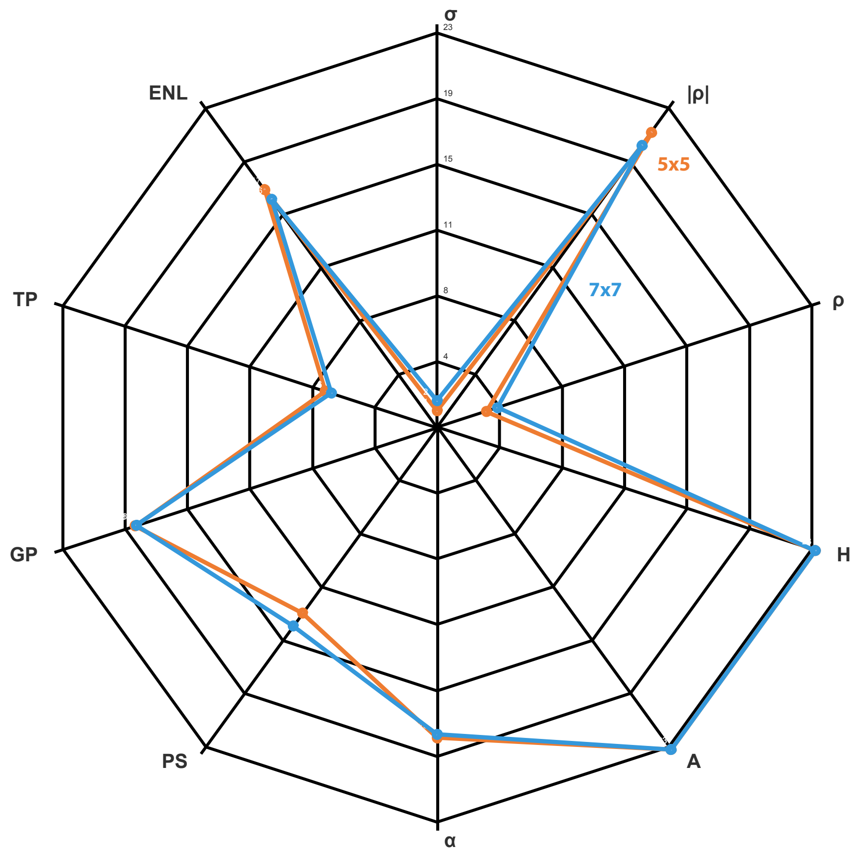

Figure 6.13: Radar Chart of Non Local Mean Sigma Filter.

The original image and the filtered images are shown in Figure 6.14.

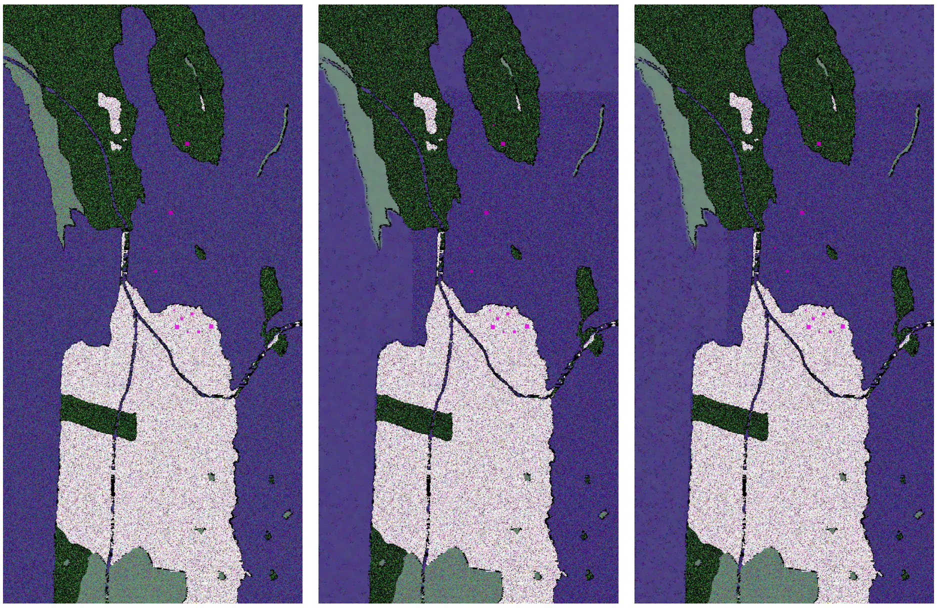

Figure 6.14: Filtering NLM Sigma: unfiltered, filtered [5x5 - 3 look], filtered [7x7 - 3 look].

6.7 Non Local Mean Refined Filter

The same concept analyzed in Section 6.6, is applied to the Lee refined filter. As the previous filter, good values of radiometric parameter σ and phase of complex correlation parameters $\angle\rho$ are found. Still comparing the NLMF of Lee and Lee refined, the second one has really better values in term of the mean angle alpha $\hat{\alpha}$, but worst values in therm of amplitude of complex correlation parameters $|\rho|$.

$\mathcal{F}$ | Δ_β	σ	$\|\rho\|$	$\angle\rho$	H	A	$\bar{\alpha}$	PS	GP	TP	ENL
NLM Refined 7	1.41	30.12	5.60	58.94	100	13.04	14.05	15.99	6.83	17.58
NLM Refined 9	1.58	21.11	6.08	56.21	100	12.57	14.65	15.85	6.83	16.32

Table 6.8: Non Local Mean Refined Filter Result.

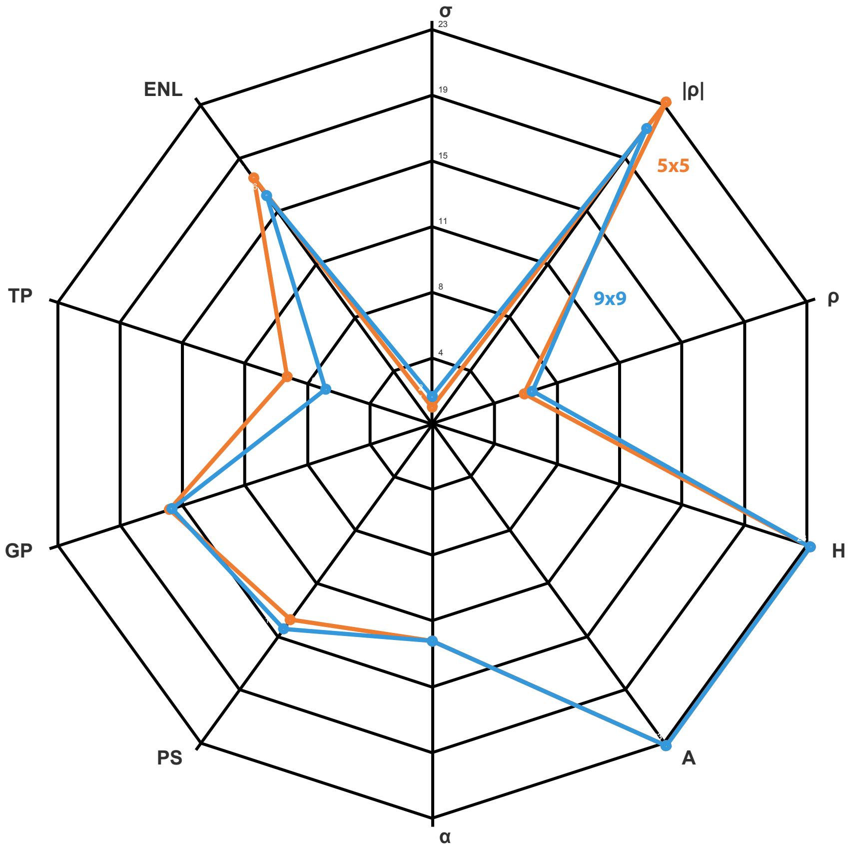

Figure 6.15: Radar Chart of Non Local Mean Refined Filter.

The original image and the filtered images are shown in Figure 6.16.

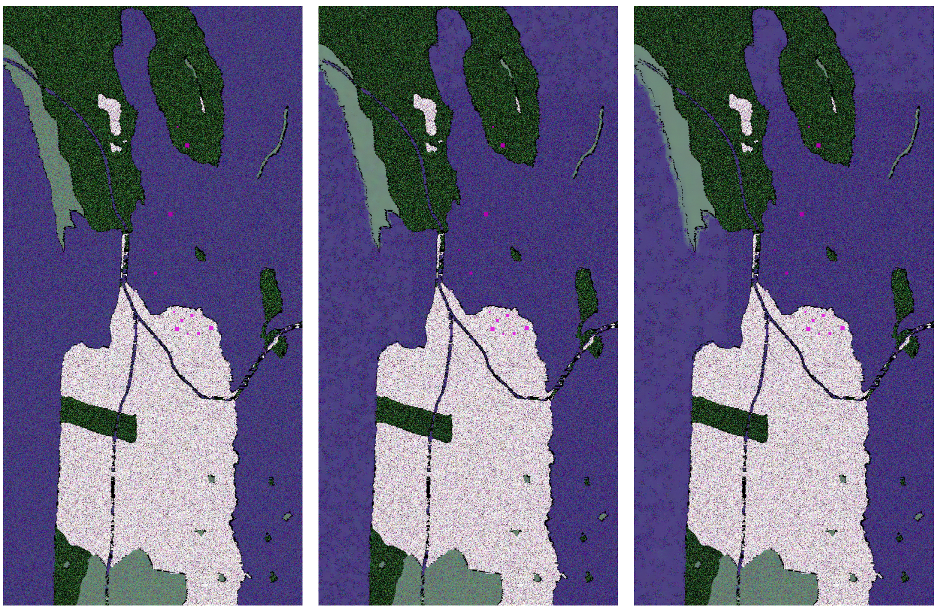

Figure 6.16: Filtering NLM Refined: unfiltered, filtered [7x7 - 3 look], filtered [9x9 - 5 look].

Conclusion 7

The whole work of this master thesis treats several and different concepts as electromagnetism, radar system, physic, remote sensing and statistics. For this reason a large part of the work has been deep understand the theory behind the concepts concepts needed. On the base of the results found during the research near the *University of Trømso*, some more step will be made subsequently. The main step will be to use the informations acquired for realizing a new PolSAR filter and then to use the parameters previous defined for comparing the new filtering result with the other.

First, in the *data simulation* chapter have been added two improvements compared to the article [4], where this work has its basis.

- An image was created whose shape approximates a real image. Thus, the spatial parameter could be tested and the numeric results can be more easy visually compared to the filtered images.
- The synthetic image has the contributions of two kind of texture. The first in the urban area and the second in the forest area. Texture is necessary to give a fingerprint of realistic statistic distribution of the simulated image.

Secondly, following [4] in the *data analysis* chapter, have been created ten parameters for evaluating the PolSAR image. Evaluation parameters with different task are useful to have a global view of the filtering operation.

Finally, the analysis and comparison of the *result* chapter, returns some clarification about PolSAR filtering. It is clear that is not possible to simply choose a filter compared to another, but the choice must be made on the base of the information to preserve. That means specific good estimation of parameters for each choice. Moreover, there are intrinsic properties that change the filtering result and then the estimation as well. In a general way, where there is not a specific parameter information to preserve, has been found a filter which is able to give back an amount of better estimation compared to the other. The filter in question is the *Lopez filter* and the estimation previous cited are in term of: entropy H, anisotropy A, the mean of the angle alpha $\hat{\alpha}$, the preservation of polarization signature PS, the preservation gradient GP and the equivalent number of looks ENL. Moreover, in summary, the *Gaussian filter* has the best value of the amplitude of complex correlation $|\rho|$, *Lee filter* has the best value of point target preservation TP, *Lee Refined* has the best value of the phase of complex correlation $\angle\rho$ and finally *NLM Sigma filter* has the best value of the radiometric preservation σ.

Other improvements in this field may be:

- Generating a synthetic image using both the concepts of MRF and to hold a real shape. The MRF is useful to improve the randomness of the data and then the reliability of the estimation parameters.
- Changing the texture distribution seen in Section 4.2.3, using the cases less widely used in literature.
- Wide-spectrum investigation about some unexpected behaviour of the parameters, as the saturation of H/A.
- Specific tests about point target preservation in urban areas, which returns more distortion.

Bibliography

[1] E. Chuvieco and A. Huete, *Fundamentals of Satellite Remote Sensing*. CRC Press, 2009.

[2] I. G. Cumming and F. H. chee Wong, *Digital Processing of Synthetic Aperture Radar Data: Algorithms and Implementation*. Artech House, 2005, vol. 1.

[3] S. B. Lucioano Alparone, Burno Aiazzi and A. Garzelli, *Remote Sensing Image Fusion*. CRC Press, March 2015.

[4] S. Foucher and C. López-Martínez, "Analysis, evaluation, and comparison of polarimetric sar speckle filtering techniques," *IEEE Transactions on Image Processing*, vol. 23, no. 4, p. 1751, April 2014.

[5] J.-S. Lee and E. Pottier, *Polarimetric Radar Imaging from Basics to Applications*. CRG Press, 2009.

[6] G. Franceschetti, *Campi elettromagnetici*, B. Boringhieri, Ed., February 1983.

[7] *Electromagnetic Waves and Antennas*. Sophocles J. Orfanidis, August 2016.

[8] C. A. Balanis, *Antenna Theory Analysis and Design*. Wiley-Interscience, 2015.

[9] E. Chuvieco, *Fundamentals of Satellite Remote Sensing: An Environmental Approach*, 2nd ed. CRC Press, 2010.

[10] M. Y. G. K. I. H. Alberto Moreira, Pau Prats-Iraola and K. P. Papathanassiou, "A tutorial on synthetic aperture radar," *IEEE Geoscience and Remote Sensing Magazine*, vol. 1, no. 1, pp. 6–43, March 2013.

[11] J. van Zyl and Y. Kim, *Synthetic Aperture Radar Polarimetry*. Wiley-Interscience, 2010.

[12] M. I. Skolnim, *Introduction to Radar System*. McGraw-Hill, May 2001.

[13] J. R. Huynen, *Phenomenological theory of radar targets*. Drukkerij Bronder-Offset N.V., 1970.

[14] EartESA. (2017) Polarimetry tutorial. [Online]. Available: https://earth.esa.int/web/polsarpro/polarimetry-tutorial

[15] R. K. S.V. Nghiem, S.H. Yueh and F. Li, "Symmetry properties in polarimetric remote sensing," *Radio Science*, vol. 27, no. 5, pp. 693–711, 1992.

[16] S. R. Cloude and E. Pottier, "An entropy based classification scheme for land applications of polarimetric sar," *IEEE Transactions on Geoscience and Remote Sensing*, vol. 35, no. 1, pp. 68–78, January 1997.

[17] J. K. Jong-Sen Lee, Thomas Ainworth and C. López-Martínez, “Statistical evaluation end bias removal of multi-look effect on entropy/alpha/anisotropy in polarimetric target decomposition,” *IEEE Transactions on Geoscience and Remote Sensing*, vol. 46, no. 10, pp. 3039–3052, October 2008.

[18] J. W. Goodman, “Some fundamental properties of speckle,” *Journal of the Optical Society of America*, vol. 66, no. 11, pp. 1145–1150, November 1976.

[19] A. L. Fabrizio Argenti and L. Alparone, “A tutorial on speckle reduction in synthetic aperture radar images,” *IEEE Geoscience and Remote Sensing Magazine*, vol. 1, no. 3, pp. 6–35, September 2013.

[20] E. Lefebvre, *Advances and Challenges in Multisensor Data and Information Processing*. IOS Press, 2007.

[21] C. Oliver and S. Quegan, *Understanding Synthetic Aperture Radar Images*. SciTech Publishing, Inc., 2004.

[22] T. F. H. F. T. Ulaby and R. T. Austin, “Fluctuation statistics of millimeter-wave scattering from distributed targets,” *IEEE Transactions on Geoscience and Remote Sensing*, vol. 26, no. 3, pp. 268–281, May Fluctuation statistics of millimeter-wave scattering from distributed targets.

[23] A. Papoulis and S. U. Pillai, *Probability, Random Variables, and Stochastic Processes*, 4th ed. McGraw-Hill Higher Education, 2002.

[24] T. Eltoft, “The rician inverse gaussian distribution: A new model for non-rayleigh signal amplitude statistics,” *IEEE Transactions on Image Processing*, vol. 14, no. 11, pp. 1722–1735, November 2005.

[25] NASA. (2008, August) Airsar. [Online]. Available: https://airsar.jpl.nasa.gov/

[26] S. R. Cloude and E. Pottier, “A review of target decomposition theorems in radar polarimetry,” *IEEE Transactions on Geoscience and Remote Sensing*, vol. 34, no. 2, p. 498, March 1996.

[27] L. M. Novak and M. C. Burl, “Optimal speckle reduction in polarimetric sar imagery,” *IEEE Transactions on Aerospace and Electronic System*, vol. 26, no. 2, pp. 293–305, March 1990.

[28] J.-S. Lee and M. R. Grunes, “Classification of multi-look polarimetric sar imagery based on complex wishart distribution,” *Telesystems Conference*, May 1992.

[29] A. P. Doulgeris, “Statistical modelling of polarimetric sar data,” Department of Physics, University of Tromsø, N-9037 Tromsø, Norway, May 2006.

[30] R. L. J.S. Lee, D.L. Schuler and K. Ranson, “K-distribution for multi-look processed polarimetric sar imagery,” *IEEE International Geoscience and Remote Sensing Symposium*, pp. 2179–2181, 1994.

[31] A. N. Allessio Balleri and J. Wang, “Maximum likelihood estimation for compound-gaussian clutter with inverse gamma texture,” *IEEE Transactions On Aerospace And Electronic Systems*, vol. 43, no. 2, pp. 775–780, April 2007.

[32] V. K. Esa Ollila, David E. Tyler and H. V. Poor, “Compound-gaussian clutter modeling with an inverse gaussian texture distribution,” *IEEE Signal Processing Letters*, vol. 19, no. 12, pp. 876–879, December 2012.

[33] D. D. Jay Emmanuelle, Ovarlez Jean-Philippe and D. Patrick, “Bayesian optimum radar detector in non·gaussian noise,” *IEEE International Conference on Acoustics, Speech, and Signal Processing*, pp. 1289–1292, May 2002.

[34] J. G. José Naranjo Torres and A. C. Frery, “Region discrimination in sar imagery using the geodesic distance between g0 distributions,” *IEEE Asia-Pacific Conference on Synthetic Aperture Radar*, pp. 573–577, September 2015.

[35] M. Quartulli and M. Datcu, “Stochastic geometrical modeling for built-up area understanding from a single sarintensity image with meter resolution,” *IEEE Transactions on Geoscience and Remote Sensing*, vol. 42, no. 9, pp. 1996–2003, September 2004.

[36] L. Bombrun and J.-M. Beaulieu, “Fisher distribution for texture modeling of polarimetric sar data,” *IEEE Geoscience and Remote Sensing Letters*, vol. 5, no. 3, pp. 512–516, July 2008.

[37] J. B. Ridha Touzi, Armand Lopes and P. W. Vachon, “Coherence estimation for sar imagery,” *IEEE Transactions on Geoscience and Remote Sensing*, vol. 37, no. 1, pp. 135–149, January 1999.

[38] J. van Zyl, H. A. Zebker, and C. Elachi, “Imaging radar polarization signatures theory and observation,” *Radio Science*, vol. 22, no. 4, pp. 529–543, July-August 1987.

[39] W. P. Biao Zhang and Y. H. G. 2010], “Validation of radarsat-2 fully polarimetric sar measurements of ocean surface waves,” *Geophysical Research*, vol. 115, 2010.

[40] J.-S. L. Dale L. Schuler and K. W. Hoppel, “Polarimetric sar image signatures of the ocean and gulf stream features,” *IEEE Transactions on Geoscience and Remote Sensing*, vol. 31, no. 6, pp. 1210–1221, November 1993.

[41] Y. Yu and S. T. Acton, “Speckle reducing anisotropic diffusion,” *IEEE Transactions on Image Processing*, vol. 11, no. 11, pp. 1260–1270, November 2002.

[42] W. K. Pratt, *Digital Image Processing*. Wiley-Interscience, 1978.

[43] G. A. Pierre Charbonnier, Laure Blanc-Féraud and M. Barlaud, “Deterministic edge-preserving regularization in computed imaging,” *IEEE Transactions on Image Processing*, vol. 6, no. 2, pp. 298–311, February 1997.

[44] A. P. D. Stian Normann Anfinsen and T. Eltoft, “Estimation of the equivalent number of looks in polarimetric synthetic aperture radar imagery,” *IEEE Transactions on Geoscience and Remote Sensing*, vol. 47, no. 11, pp. 3795–3809, November 2009.

[45] T. L. A. K.-S. C. Jong-Sen Lee, Jen-Hung Wen and A. J. Chen, “Improved sigma filter for speckle filtering of sar imagery,” *IEEE Transactions on Geoscience and Remote Sensing*, vol. 47, no. 1, pp. 202–213, January 2009.

[46] D. Massonnet and J.-C. Souyris, *Imaging With Synthetic Aperture Radar*. CRC Press, 2008.

[47] F. Henderson and A. Lewis, *Principles and Applications of Imaging Radar. Manual of remote sensing: Third edition, Volume 2*. John Wiley and Sons, Inc., Somerset, NJ (United States), December 1998.